Algorithm Theoretical Baseline for formaldehyde retrievals from S5P TROPOMI and from the QA4ECV project.

Isabelle De Smedt[1], Nicolas Theys[1], Huan Yu[1], Thomas Danckaert[1], Christophe Lerot[1], Steven Compernolle[1], Michel Van Roozendael[1], Andreas Richter[2], Andreas Hilboll[2], Enno Peters[2], Mattia Pedergnana[3], Diego Loyola[3], Steffen Beirle[4], Thomas Wagner[4], Henk Eskes[5], Jos van Geffen[5], Klaas Folkert Boersma[5,6], Peepijn Veefkind[5].

[1]{Royal Belgian Institute for Space Aeronomy (BIRA-IASB), Brussels, Belgium}

[2]{Institute of Environmental Physics, University of Bremen (IUP-B), Otto-Hahn-Allee 1, 28359 Bremen, Germany}

[3]{Institut für Methodik der Fernerkundung (IMF), Deutsches Zentrum für Luft und Raumfahrt (DLR), Oberpfaffenhofen, Germany}

[4]{ Max Planck Institute for Chemistry (MPIC), Hahn-Meitner-Weg 1, 55128 Mainz, Germany}

[5]{KNMI, De Bilt, The Netherlands}

[6]{Wageningen University, Meteorology and Air Quality group, Wageningen, The Netherlands}

Correspondence to: I. De Smedt (isabelle.desmedt@aeronomie.be)

Abstract: On board of the Copernicus Sentinel-5 Precursor (S5P) platform, the TROPOspheric Monitoring Instrument (TROPOMI) is a double channel nadir-viewing grating spectrometer measuring solar back-scattered earthshine radiances in the ultraviolet, visible, near-infrared and shortwave infrared with global daily coverage. In the ultraviolet range, its spectral resolution and radiometric performance are equivalent to those of its predecessor OMI, but its horizontal resolution at true nadir is improved by an order of magnitude. This paper introduces the formaldehyde (HCHO) tropospheric vertical column retrieval algorithm implemented in the S5P operational processor, and comprehensively describes its various retrieval steps. Furthermore, algorithmic improvements developed in the framework of the EU FP7-project QA4ECV are described for future updates of the processor. Detailed error estimates are discussed in the light of Copernicus user requirements and needs for validation are highlighted. Finally, verification results based on the application of the algorithm to OMI measurements are presented, demonstrating the performances expected for TROPOMI.

1. Introduction

Long term satellite observations of tropospheric formaldehyde (HCHO) are essential to support air quality and chemistry-climate related studies from the regional to the global scale. Formaldehyde is an intermediate gas in almost all oxidation chains of non-methane volatile organic compounds (NMVOC), leading eventually to CO_2 (Seinfeld and Pandis, 2006). NMVOCs are, together with NO_x, CO and CH_4, among the most important precursors of tropospheric ozone. NMVOCs also produce secondary organic aerosols and influence the concentrations of OH, the main tropospheric oxidant (Hartmann et al., 2013). The major HCHO source in the remote atmosphere is CH_4 oxidation. Over the continents, the oxidation of higher NMVOCs emitted from vegetation, fires, traffic and industrial sources results in important and localised enhancements of the HCHO levels (as illustrated in Figure 1, Stavrakou et al., 2009a). With its lifetime of the order of a few hours, HCHO concentrations in the boundary layer can be related to the release of short-lived hydrocarbons, which mostly cannot be observed directly from space. Furthermore, HCHO observations provide information on the chemical oxidation processes in the atmosphere, including CO chemical production from CH_4 and NMVOCs. The
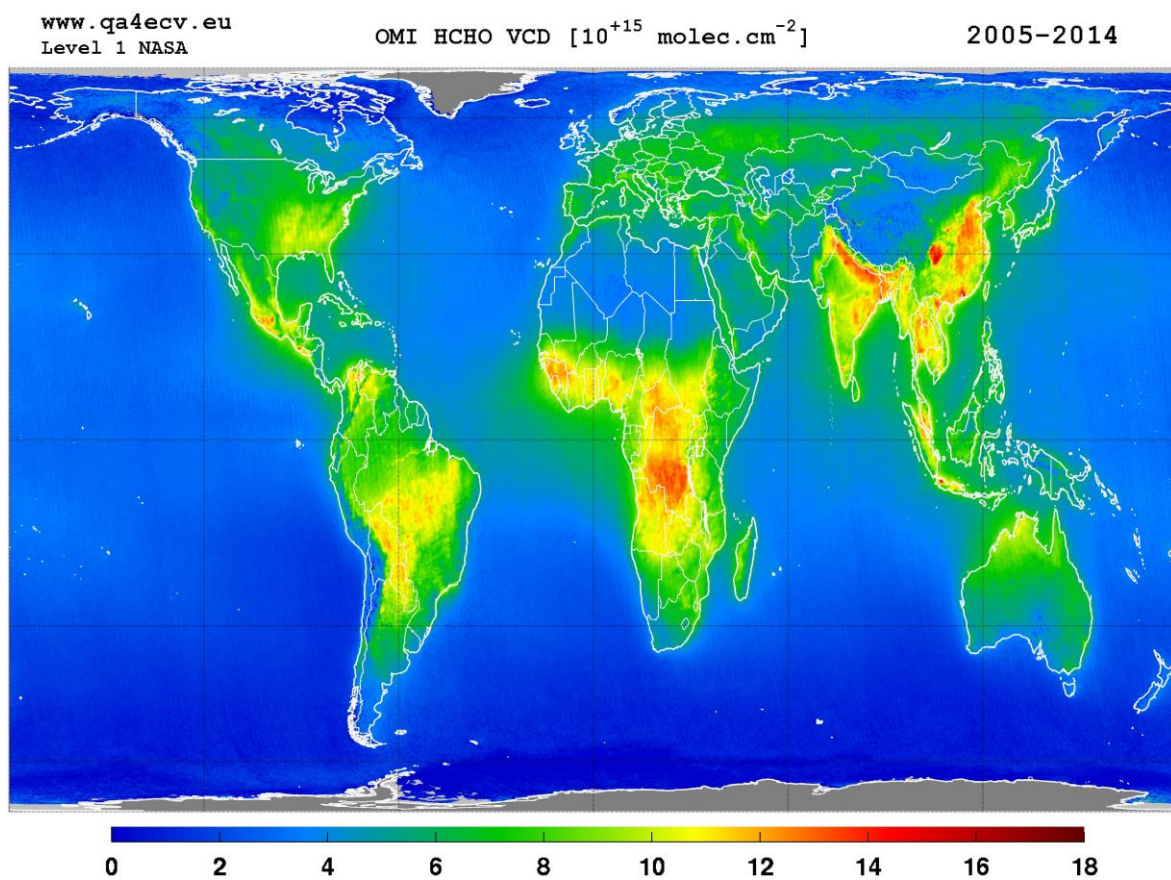
seasonal and inter-annual variations of the formaldehyde distribution are principally related to temperature changes (controlling vegetation emissions) and fire events, but also to changes in anthropogenic activities (Stavrakou et al., 2009b). For all these reasons, HCHO satellite observations are used in combination with tropospheric chemistry transport models to constrain NMVOC emission inventories in so-called top-down inversion approaches (e.g. Abbot et al., 2003, Palmer et al., 2006; Fu et al., 2007; Millet et al., 2008; Stavrakou et al., 2009a, 2009b, 2012, 2015; Curci et al., 2010; Barkley et al., 2011, 2013: Fortems-Cheiney et al., 2012; Marais et al., 2012; Mahajan et al., 2015; Kaiser et al., 2017).

HCHO tropospheric columns have been successively retrieved from GOME on ERS-2 and from SCIAMACHY on ENVISAT, resulting in a continuous data set covering a period of almost 16 years from 1996 until 2012 (Chance et al., 2000; Palmer et al., 2001; Wittrock et al., 2006; Marbach et al., 2009; De Smedt et al., 2008; 2010). Started in 2007, the measurements made by the three GOME-2 instruments (EUMETSAT METOP-A, B and C) have the potential to extend by more than a decade the successful time-series of global formaldehyde morning observations (Vrekoussis et al., 2010; De Smedt et al., 2012; Hewson et al., 2012; Hassinen et al., 2016). Since its launch in 2004, OMI on the NASA AURA platform has been providing complementary HCHO measurements in the early afternoon with daily global coverage and a better spatial resolution than current morning sensors (Kurosu et al., 2008; Millet et al., 2008; González Abad et al., 2015; De Smedt et al., 2015). On the S-NPP spacecraft, OMPS also allows to retrieve HCHO columns since the end of 2011 (Li et al., 2015; González Abad, 2016). TROPOMI aims to continue this time series of early afternoon observations, with daily global coverage, a spectral resolution and signal-to-noise ratio (SNR) equivalent to OMI, but combined with a spatial resolution improved by an order of magnitude, which potentially offers an unprecedented view of the spatiotemporal variability of NMVOC emissions.

To fully exploit the potential of satellite data, applications relying on tropospheric HCHO observations require high quality long-term time series, provided with well characterized errors and averaging kernels, and consistently retrieved from the different sensors. Furthermore, as the HCHO observations are aimed to be used synergistically with other species observations (e.g. with NO_2 for air quality applications), it is essential to homogenize as much as possible the retrieval methods as well as the external databases, in order to minimize systematic biases between the observations. The design of the TROPOMI HCHO prototype algorithm, developed at BIRA-IASB, has been driven by the experience developed with formaldehyde retrievals from the series of precursor missions OMI, GOME(-2) and SCIAMACHY. Furthermore, within the S5P Level 2 Working Group project (L2WG), a strong component of verification has been developed involving independent retrieval algorithms for each operational prototype algorithm. For HCHO, the University of Bremen (IUP-UB) has been responsible of the algorithm verification. An extensive comparison of the processing chains of the prototype (the retrieval algorithm presented in this paper) and verification algorithm has been conducted. In parallel, within the EU FP7-project Quality Assurance for Essential Climate Variables (QA4ECV, Lorente et al., 2017), a detailed step by step study has been performed for HCHO and NO_2 DOAS retrievals, including more scientific algorithms (BIRA-IASB, IUP-UB, MPIC, KNMI and WUR), leading to state-of-the art European products (www.qa4ecv.eu). Those iterative processes led to improvements that have been included in the S5P prototype algorithm, or are proposed as options for future improvements of the operational algorithm.

This paper gives a thorough description of the TROPOMI HCHO algorithm baseline, as implemented at the German Aerospace Center (DLR) in the S5P operational processor UPAS-2 (Universal Processor for UV/VIS Atmospheric Spectrometers). It reflects the S5P HCHO Level 2 Algorithm Theoretical Basis Document v1.0 (De Smedt et al., 2016) and also describes the options to be activated after the S5P launch, as implemented for the QA4ECV OMI HCHO retrieval algorithm (see illustration in Figure 1).

In Section 2, we discuss the product requirements and the expected product performance in terms of precision and trueness, and provide a complete description of the retrieval algorithm. In Section 3, the uncertainty of the retrieved columns and the error budget is presented. Results from the algorithm verification exercise are given in Section 4. The possibilities and needs for future validation of the retrieved HCHO data product can be found in Section 5. Conclusions are given in Section 6.

Figure 1: 10-years average of HCHO vertical columns retrieved from OMI between 2005 and 2014 (http://www.qa4ecv.eu/ecv/hcho-p/data).

2. TROPOMI HCHO algorithm

2.1 Product Requirements

In the UV, the sensitivity to HCHO concentrations in the boundary layer is intrinsically limited from space due to the combined effect of Rayleigh and Mie scattering that limit the fraction of radiation scattered back from low altitudes and reflected from the surface to the satellite. In addition, ozone absorption reduces the number of photons that reach the lowest atmospheric layers. Furthermore, the absorption signatures of HCHO are weaker than those of other UV-Vis absorbers, such as e.g. NO_2. As a result, the retrieval of formaldehyde from space is noise sensitive and error prone. While the precision (or random uncertainty) is mainly driven by the signal to noise ratio of the recorded spectra, the trueness (or systematic uncertainty) is limited by the current knowledge on the external parameters needed in the different retrieval steps.

The requirements for HCHO retrievals have been identified as part of the TROPOMI science objectives document (van Weele et al., 2008), the COPERNICUS Sentinels-4/-5 Mission Requirements Document MRD (Langen et al., 2011; 2017), and the S5P Mission Advisory Group report of the review of user requirements for Sentinels-4/-5 (Bovensmann et al., 2011). The requirements for HCHO are summarised in Table 1. Uncertainty requirements include retrieval errors as well as measurement (instrument-related) errors. Absolute requirements (in total column units) relate to background conditions, while percentage values relate to elevated columns.
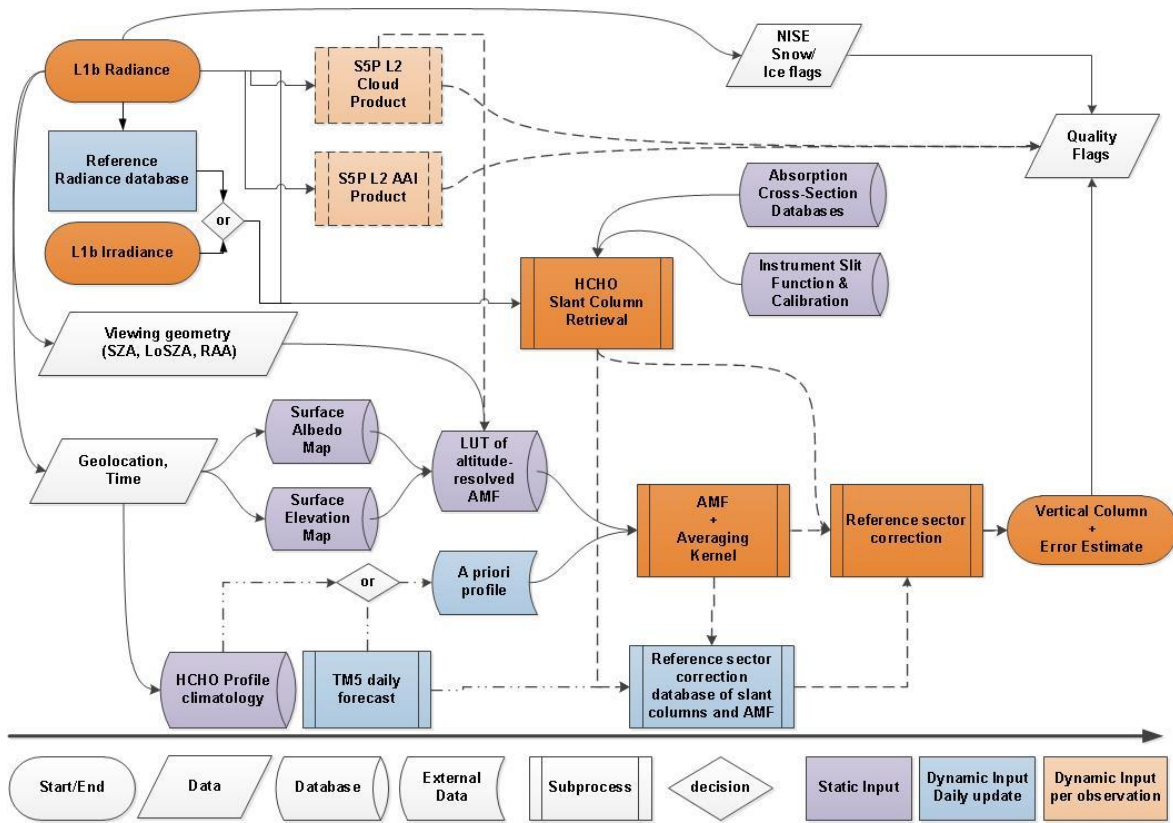
Three main COPERNICUS environmental themes have been defined as ozone layer (A), air quality (B), and climate (C) with further division into sub themes. Requirements for HCHO have been specified for a number of these sub themes (B1: Air Quality Protocol Monitoring, B2: Air Quality Near-Real Time, B3: Air Quality Assessment, and C3: Climate Assessment). With respect to air quality protocol monitoring, which is mostly concerned with trend and variability analysis, the requirements are specified for NMVOC emissions on monthly to annual time scales and for larger region/country scale (Bovensmann et al., 2011). In the error analysis section, we discuss these requirements and the expected performances of the HCHO retrieval algorithm.

Table 1: Requirements on HCHO vertical tropospheric column products as derived from the MRD. Where numbers are given as "a - b", the first is the target requirement and the second is the threshold requirement.

Horizontal resolution	Revisit time	Theme	Required uncertainty
5-20 km	0.5-2 hour	B1, B2, B3	30-60% or 1.3×10^{15} molec.cm^{-2} (least stringent)
5-50 km	6 - 24x3 hour	C3	30% or 1.3×10^{15} molec.cm^{-2} (least stringent)

2.2 Algorithm description

Figure 2: Flow Diagram of the L2 HCHO retrieval algorithm implemented in the S5P operational processor.

Figure 2 displays a flow diagram of the level-2 (L2) HCHO retrieval algorithm implemented in the S5P operational processor. The baseline operation flow scheme is based on the Differential Optical Absorption Spectroscopy (DOAS) retrieval method (Platt et al., 1994; Platt and Stutz, 2008; and references therein). It is identical in concept to the one of SO_2 (Theys et al., 2017) and very close to the one of NO_2 (van Geffen et al., 2017). The interdependencies with auxiliary data and other L2 retrievals, such as clouds, aerosols or surface reflectance are also represented.

Following the diagram in Figure 2, the processing of S5P level-1b (L1b) data proceeds as follows: radiance and irradiance spectra are read from the L1b file, along with geolocation data such as pixel coordinates and observation geometry (sun and viewing angles). The relevant absorption cross section data as well as characteristics of the instrument are used as input for the determination of the HCHO slant columns (N_s). In parallel to the slant column fit, S5P cloud information and absorbing aerosol index (AAI) data are obtained from the operational chain. Alongside, in order to convert the slant column to a vertical column (N_v), an air mass factor (M) that accounts for the average light path through the atmosphere is calculated. For this purpose, several auxiliary data are read from external (operational and static) sources: cloud cover data, topographic information, surface albedo, and the a priori shape of the vertical HCHO profile in the atmosphere. The AMF is computed by combining an a priori formaldehyde vertical profile and altitude-resolved air mass factors extracted from a pre-computed look-up-table (also used as a basis for the error calculation and retrieval characterization module). This look up table has been created using the VLIDORT 2.6 radiative transfer model

141 (Spurr et al., 2008a) at a single wavelength representative for the retrieval interval. It is used to compute the
142 total column averaging kernels (Eskes and Boersma, 2003), which provide essential information on the
143 measurement vertical sensitivity and are required for comparison with other types of data.

144 Background normalization of the slant columns is required in the case of weak absorbers such as formaldehyde.
145 Before converting the slant columns into vertical columns, background values of N_s are normalized to
146 compensate for possible systematic offsets (reference sector correction, see below). The tropospheric vertical
147 column end product results therefore from a differential column to which is added the HCHO background due
148 to methane oxidation, estimated using a tropospheric chemistry transport model.

149 The final tropospheric HCHO vertical column is obtained using the following equation:

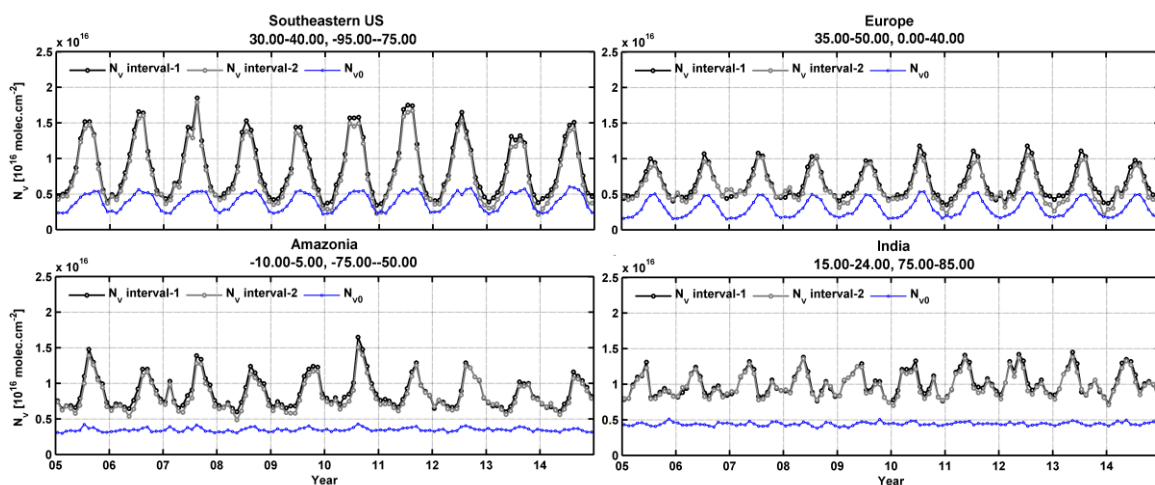$$N_v = \frac{N_s - N_{s,0}}{M} + N_{v,0}$$

(1)

150 The main outputs of the algorithm are the slant column density (N_s), the tropospheric vertical column (N_v), the
151 tropospheric air mass factor (M), and the values used for the reference sector correction ($N_{s,0}$ and $N_{v,0}$).
152 Complementary product information includes the clear sky air mass factor, the uncertainty on the total column,
153 the averaging kernel, and quality flags. Table 13 in the appendix B gives a non-exhaustive set of data fields
154 that are provided in the level 2 data product. A complete description of the level 2 data format is given in the
155 S5P HCHO Product User Manual (Pedergnana et al., 2017).

156 Algorithmic steps are described in more details in the next sections, and settings are summarized in Table 2,
157 along with algorithmic improvements developed in the framework of the EU FP7-project QA4ECV and
158 proposed for future TROPOMI processor updates. Figure 3 presents examples of monthly averaged HCHO
159 vertical columns over four NMVOC emission regions, along with the background correction values.

160 **Table 2 : Summary of algorithm settings used to retrieve HCHO tropospheric columns from**
161 **TROPOMI spectra. The last column lists additional features implemented in the QA4ECV HCHO**
162 **product, which are options for future updates of the S5P Processor.**

Parameter	S5P Operational Algorithm	QA4ECV Algorithm
Slant Columns		
Fitting interval-1	328.5-359 nm	
Fitting interval-2	328.5-346 nm ($N_{s,\,BrO}$ fixed by fit in interval-1)	
Absorption cross-sections	HCHO, Meller and Moortgat (2000), 298K NO_2, Vandaele et al. (1998), 220K Ozone, Serdyuchenko et al. (2013), 223 + 243K BrO, Fleischmann et al. (2004), 223K O_2-O_2, Thalman et al. (2013), 293K	
Ring effect	Ring cross-section based on the technique outlined by Chance et al. (1997), defined as I_{rrs}/I_{elas}, where I_{rrs} and I_{elas} are the intensities for inelastic (Rotational Raman Scattering; RRS) and elastic scattering processes.	
Non-linear O3 absorption effect	2 pseudo-cross sections from the Taylor expansion of the ozone slant column into wavelength and the O_3 vertical optical depth (Puķīte et al., 2010).	

Slit function	One slit function per binned spectrum as a function of wavelength (Pre Flight Model, TROPOMI ISRF Calibration Key Data v1.0.0)	Fit of a prescribed function shape to determine the ISRF during wavelength calibration + online convolution of cross-sections.
Polynomial	5th order	
Intensity offset correction	Linear offset ($1/I_0$)	
Iterative spike removal	Not activated.	Activated. Tolerance factor 5 (see section 2.2.1)
Reference spectrum I_0	Daily solar irradiance	Daily average of radiances, per row, selected in a remote region.
Air Mass Factors		
Altitude dependent AMFs	VLIDORT , 340 nm, 6-D AMF look-up table	
Treatment of partly cloudy scenes	IPA, no correction for f_{eff} <10%	
Aerosols	No explicit correction	
A priori profile shapes	TM5-MP 1°x1°, daily forecast (NRT) or reprocessed (Offline)	
Correction of surface pressure	Yes (Equation (10))	
Surface Albedo	OMI-based monthly minimum LER (update of Kleipool et al., 2008)	
Digital elevation map	GMTED2010 (Danielson et al., 2011)	
Cloud product	S5P operational cloud product, treating clouds as Lambertian reflectors (OCRA/ROCINN-CRB, Loyola et al., 2017)	OMI operational cloud algorithm, treating clouds as Lambertian reflectors (O_2-O_2 , Veefkind et al., 2016)
Background Correction		
Correction equation	$N_{v,0} = N_{v,0,CTM}$	$N_{v,0} = \frac{M_0}{M} N_{v,0,CTM}$ (see section 2.2.3)

163

Figure 3: Example of regional and monthly averages of the HCHO vertical columns over different NMVOC emission regions, derived from OMI observations for the period 2005-2014. Results of the

7

166　**retrievals in the two fitting intervals (1:328.5-359 nm and 2: 328.5-346 nm, with BrO fitted in interval-**
167　**1) are shown, as well as the magnitude of the background vertical column ($N_{v,0}$).**

168　**2.2.1 Formaldehyde slant column retrieval**

169　The DOAS method relies on the application of Beer-Lambert's law. The backscattered earthshine spectrum as
170　measured by the satellite spectrometer contains the strong solar Fraunhofer lines and additional fainter features
171　due to interactions taking place in the Earth atmosphere during the incoming and outgoing paths of the
172　radiation. The basic idea of the DOAS method is to separate broad and narrowband spectral structures of the
173　absorption spectra in order to isolate the narrow trace gas absorption features. In practice, the application of
174　the DOAS approach to scattered light observations relies on the following key approximations:

175　　　1.　　For weak absorbers the exponential function can be linearized and the Lambert-Beer law can be
176　　　　　applied to the measured radiance to which a large variety of atmospheric light paths contributes.
177　　　2.　　The absorption cross-sections are assumed to be weakly dependent on temperature and
178　　　　　independent of pressure. This allows expressing light attenuation in terms of Beer-Lambert's law,
179　　　　　and (together with approximation 1) separating spectroscopic retrievals from radiative transfer
180　　　　　calculations by introducing the concept of one effective slant column density for the considered
181　　　　　wavelength window.
182　　　3.　　Broadband variations are approximated by a common low-order polynomial to compensate for
183　　　　　the effects of loss and gain from scattering and reflections by clouds/air molecules and/or at the
184　　　　　Earth surface.

185　The DOAS equation is obtained by considering the logarithm of the radiance $I(\lambda)$ and the irradiance $E_0(\lambda)$ (or
186　another reference radiance selected in a remote sector) and including all broadband variations in a polynomial
187　function:

$$\ln \frac{I(\lambda)}{E_0(\lambda)} \cong - \sum_j \sigma_j(\lambda) \, N_{s,j} + \sum_p c_p \lambda^p \tag{2}$$

$$\tau_s^{meas}(\lambda) \cong \tau_s^{diff}(\lambda, N_{s,j}) + \tau_s^{smooth}(\lambda, c_p), \tag{3}$$

188　where the measured optical depth τ_s^{meas} is modelled using a highly structured part τ_s^{diff} and a broadband
189　variation τ_s^{smooth}.

190　Equation (2) is a linear equation between the logarithm of the measured quantities (*I* and *E₀*), the slant column
191　densities of all relevant absorbers ($N_{s,j}$) and the polynomial coefficients (c_p), at multiple wavelengths. DOAS
192　retrievals consist in solving an over-determined set of linear equations, which can be done by standard methods
193　of linear least squares fit (Platt and Stutz, 2008). The fitting process consists in minimizing the chi-square
194　function, i.e. the weighted sum of squares derived from Equation (3):
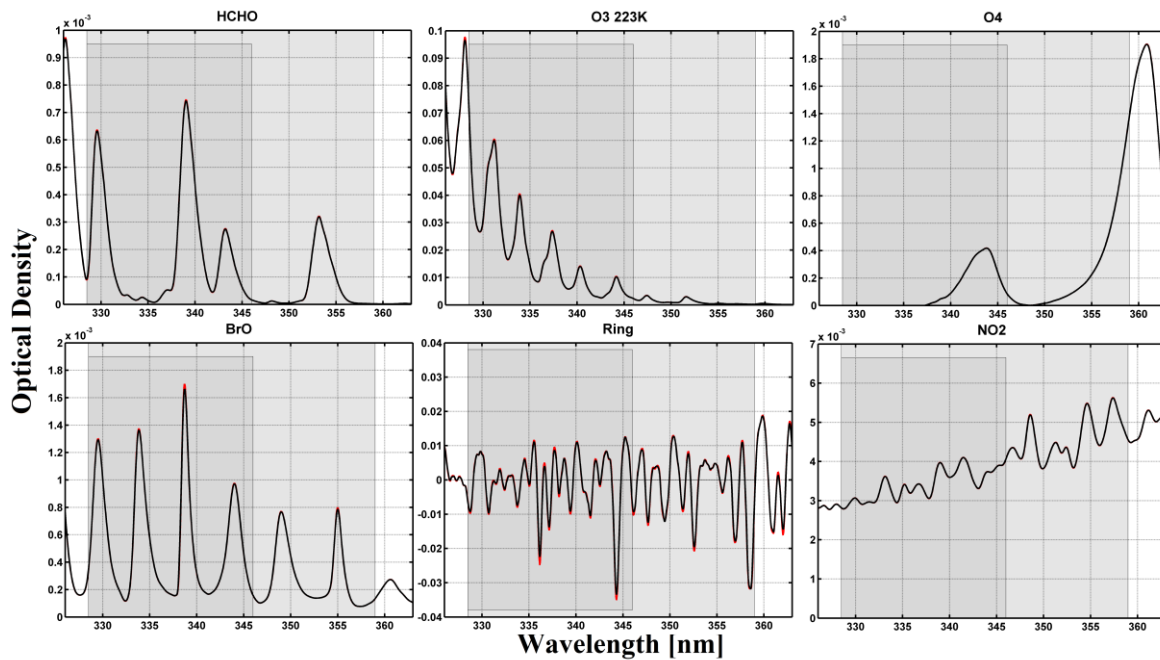
$$X^2 = \sum_{i=1}^{k} \frac{\left(\tau_s^{meas}(\lambda_i) - \tau_s^{diff}(\lambda_i, N_{s,j}) - \tau_s^{smooth}(\lambda_i, c_p)\right)^2}{\varepsilon_i^2} \tag{4}$$

195   where the summation is made over the individual spectral pixels included in the selected wavelength range (k

196   is the number of spectral pixels in the fitting interval). ε_i is the statistical uncertainty on the measurement at

197   wavelength λ_i. Weighting the residuals by the instrumental errors ε_i is optional. When no measurement

198   uncertainties are used (or no error estimates are available), all uncertainties in Equation (4) are set to $\varepsilon_i = 1$,

199   giving all measurement points equal weight in the fit.

200   In order to optimize the fitting procedure, additional structured spectral effects have to be considered carefully

201   such as the Ring effect (Grainger and Ring, 1962). Furthermore, the linearity of Equation (3) may be broken

202   down by instrumental aspects such as small wavelength shifts between I and E_0.

203   **Fitting intervals, absorption cross-sections and spectral fitting settings**

204   Despite the relatively large abundance of formaldehyde in the atmosphere (of the order of 10^{16} molec.cm^{-2})

205   and its well-defined absorption bands, the fitting of HCHO slant columns in earthshine radiances is a challenge

206   because of the low optical density of HCHO compared to other UV-Vis absorbers. The typical HCHO optical

207   density is one order of magnitude smaller than that of NO_2 and three orders of magnitude smaller than that for

208   O_3 (see Figure 4). Therefore, the detection of HCHO is limited by the signal to noise ratio of the measured

209   radiance spectra and by possible spectral interferences and misfits due to other molecules absorbing in the same

210   fitting interval, mainly ozone, BrO and O_4. In general, the correlation between cross-sections decreases if the

211   wavelength interval is extended, but the assumption of a single effective light path defined for the entire

212   wavelength interval may not be fully satisfied, leading to systematic misfit effects that may also introduce

213   biases in the retrieved slant columns. To optimize DOAS retrieval settings, a trade-off has to be found

214   minimising these effects taking also into consideration the instrumental characteristics. A basic limitation of

215   the classical DOAS technique is the assumption that the atmosphere is optically thin in the wavelength region

216   of interest. At shorter wavelengths, the usable spectral range of DOAS is limited by rapidly increasing Rayleigh

217   scattering and O_3 absorption. The DOAS assumptions start to fail for ozone slant columns larger than 1500 DU

218   (Van Roozendael et al., 2012). Historically, different wavelength intervals have been selected between 325 and

219   360 nm for the retrieval of HCHO using previous satellite UV spectrometers (e.g: GOME, Chance et al., 2000;

220   SCIAMACHY, Wittrock et al., 2006, or GOME-2, Vrekoussis et al., 2010). The TEMIS dataset combines

221   HCHO observations from GOME, SCIAMACHY, GOME-2 and OMI measurements retrieved in the same

222   interval (De Smedt et al., 2008; 2012; 2015). The NASA operational and PCA OMI algorithm exploit a larger

223   interval (Kurosu, 2008; González Abad et al., 2015, Li et al., 2015). The latest QA4ECV product uses the

224   largest interval, thanks to the good quality of the OMI level 1 spectra. A summary of the different wavelength

225   intervals is provided in Table 3.

226

Figure 4: Typical optical densities of HCHO, O$_3$, O$_2$-O$_2$, BrO, Ring effect, and NO$_2$ in the near UV. The slant columns have been taken as 1.3x10^{16} molec.cm^{-2} for HCHO, 10^{19} molec.cm^{-2} for O$_3$, 0.4x10^{43} molec^2.cm^{-5} for O$_2$-O$_2$, 10^{14} molec.cm^{-2} for BrO, and 1x10^{16} molec.cm^{-2} for NO$_2$. A ratio of 8% has been taken for Raman scattering (Ring effect). High resolution absorption cross-sections of Table 2 have been convolved with the TROPOMI ISFRs v1.0 (row 1 is shown in red and row 225 in black, see also Figure 5). The two fitting intervals (-1 and -2) used to retrieve HCHO slant columns are limited by grey areas.

Table 3: Wavelength intervals used in previous formaldehyde retrieval studies [nm].

	GOME	SCIAMACHY	GOME-2	OMI
Chance et al., 2000	337.5-359			
Wittrock et al., 2006		334-348		
Vrekoussis et al., 2010			337-353	
Hewson et al., 2012			328.5-346	
González Abad et al., 2015; Li et al., 2015				328.5-356.5
De Smedt et al., 2008 ; 2012 ; 2015	328.5-346	328.5-346	328.5-346 (BrO in 328.5-359)	328.5-346 (BrO in 328.5-359)
QA4ECV	328.5-359	328.5-359	328.5-359	328.5-359

As for the TEMIS OMI HCHO product (De Smedt et al., 2015), the TROPOMI L2 HCHO retrieval algorithm includes a two-step DOAS retrieval approach, based on two wavelength intervals:

1. 328.5-359 nm: This interval includes six BrO absorption bands and minimizes the correlation with HCHO, allowing a significant reduction of the retrieved slant column noise. Note that this interval includes part of a strong O$_4$ absorption band around 360 nm, which may introduce geophysical artefacts of HCHO columns over arid soils or high altitude regions.

2. 328.5-346 nm: in a second step, HCHO columns are retrieved in a shorter interval, but using the BrO slant column values determined in the first step. This approach allows to efficiently de-correlate BrO from HCHO absorption while, at the same time, the O_4-related bias is avoided.

The use of a large fitting interval generally allows for a reduction of the noise on the retrieved slant columns. However, a substantial gain can only be obtained if the level-1b spectra are of sufficiently homogeneous quality over the full spectral range. Indeed, experience with past sensors not equipped with polarization scramblers (e.g. GOME(-2) or SCIAMACHY) has shown that this gain can be partly or totally overruled due to the impact of interfering spectral polarization structures (De Smedt et al., 2012; 2015). Assuming spectra free of spectral features, the QA4ECV baseline option using one single large interval (fitting interval-1) will be applicable to TROPOMI, in order to further improve the precision. Results of the retrievals from the two intervals applied to OMI are presented in Figure 3. In this case, vertical column differences between the two intervals are generally lower than 10%. They can however reach 20% in winter time.

In both intervals, the absorption cross-sections of O_3 at 223K and 243K, NO_2, BrO and O_4 are included in the fit. The correction for the Ring effect, defined as I_{rrs}/I_{elas}, where I_{rrs} and I_{elas} are the intensities for inelastic (Rotational Raman Scattering; RRS) and elastic scattering processes, is based on the technique published by Chance et al. (1997). Furthermore, in order to better cope with the strong ozone absorption at wavelengths shorter than 336 nm, the method of Puķīte et al. (2010) is implemented. In this method, the variation of the ozone slant column over the fitting window is taken into account. At the first order, the method consists in adding two cross-sections to the fit: $\lambda\sigma\_O3$ and σ_O3^2 (Puķīte et al., 2010; De Smedt et al.; 2012), using the O_3 cross-sections at 223K (close to the temperature at ozone maximum in the tropics). It allows a much better treatment of optically thick ozone absorption in the retrieval and therefore to reduce the systematic underestimation of the HCHO slant columns by 50 to 80%, for SZA from 50° to 70°.

To obtain the optical density (Equation (2)), the baseline option is to use the daily solar irradiance. A more advanced option, implemented in QA4ECV, is to use daily averaged radiances, selected for each detector row, in the equatorial Pacific (Lat: [-5° 5°], Long: [180° 240°]). The main advantages of this approach are (1) an important reduction of the fit residuals (by up to 40%) mainly due to the cancellation of O_3 absorption and Ring effect present in both spectra; (2) the fitted slant columns are directly corrected for background offsets present in both spectra; (3) possible row-dependent biases (stripes) are greatly reduced by cancellation of small optical mismatches between radiance and irradiance optical channels; and (4) the sensitivity to instrument degradation affecting radiance measurements is reduced because these effects tend to cancel between the analyzed spectra and the references that are used. It must be noted however that the last three effects can be mitigated when a solar irradiance is used as reference, by means of a post-processing treatment applied as part of the background correction of the slant columns (see section 2.2.3). The option of using an equatorial radiance as reference will be activated in the operational processor after the launch of TROPOMI, during the commissioning phase of the instrument.

Wavelength calibration and convolution to TROPOMI resolution

The quality of the DOAS fit critically depends on the accuracy of the wavelength alignment between the earthshine radiance spectrum, the reference (solar irradiance) spectrum and the absorption cross sections. The wavelength registration of the reference spectrum can be fine-tuned to an accuracy of a few hundredths of a nanometer by means of a calibration procedure making use of the solar Fraunhofer lines. To this end, a reference solar atlas E_s accurate in wavelength to better than 0.01 nm (Chance and Kurucz, 2010) is degraded to the resolution of the instrument, through convolution by the TROPOMI instrumental slit function (see Figure 5).

Using a non-linear least-squares approach, the shift (Δ_i) between the TROPOMI irradiance and the reference solar atlas is determined in a set of equally spaced sub-intervals covering a spectral range large enough to encompass all relevant fitting intervals. The shift is derived according to the following equation:
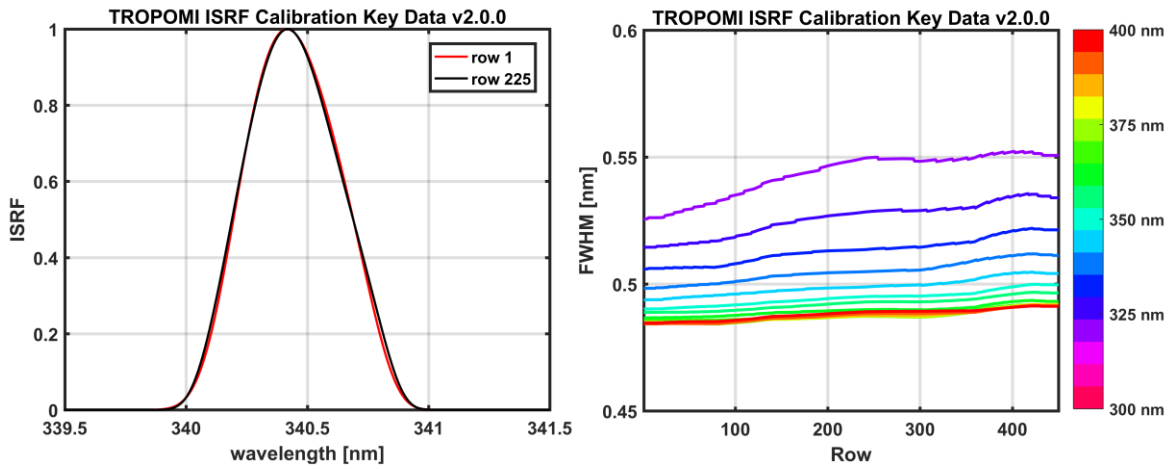
$$E_0(\lambda) = E_s(\lambda - \Delta_i)$$

(5)

where E_s is the reference solar spectrum convolved at the resolution of the TROPOMI instrument and Δ_i is the shift in sub-interval i. A polynomial is fitted through the individual points to reconstruct an accurate wavelength calibration $\Delta(\lambda)$ over the complete analysis interval. Note that this approach allows compensating for stretch and shift errors in the original wavelength assignment. In the case of TROPOMI (or OMI), the procedure is complicated by the fact that such calibrations must be performed and stored for each separate spectral field on the CCD detector array. Indeed due to the imperfect characteristics of the imaging optics, each row of the instrument must be considered as a separate detector for analysis purposes.

In a subsequent step of the processing, the absorption cross-sections of the different trace gases must be convolved with the instrumental slit functions. The baseline approach is to use slit functions determined as part of the TROPOMI key data. Slit functions, or Instrument Spectral Response Functions (ISRF), are delivered for each binned spectrum and as a function of the wavelength as illustrated in Figure 5. Note that an additional feature of the prototype algorithm allows to dynamically fit for an effective slit function of known line shape. This can be used for verification and monitoring purpose during commissioning and later on during the mission. This option is used for the QA4ECV OMI HCHO product.

More specifically, wavelength calibrations are made for each orbit as follows:

- The irradiances (one for each binned row of the CCD) are calibrated in wavelength over the 325-360 nm wavelength range, using 5 sub-windows.
- The earthshine radiances are first interpolated on the original L1 irradiance grid. The irradiance calibrated wavelength grid is assigned to those interpolated radiance values.
- The absorption cross-sections are interpolated (cubic spline interpolation) on the calibrated wavelength grid, prior to the analysis.
- In the case where averaged radiances are used as reference, an additional step must be performed: the cross-sections are aligned to the reference spectrum by means of shift/stretch values derived from a least-squares fit of the calibrated irradiance towards the averaged reference radiance.

311 • During spectral fitting, shift and stretch parameters for the radiance are derived, to align each radiance
312 with cross sections and reference spectrum.

314 **Figure 5: Right panel: Examples of TROPOMI slit functions around 340 nm, for row 1 and row 225.**
315 **Left panel: TROPOMI spectral resolution in channel 3, as a function of the row and the wavelength,**
316 **derived from the instrument key data ISFR v2.0.0.**

318 **Spike removal algorithm**

319 A method to remove individual hot pixels or pixels affected by the South Atlantic Anomaly has been presented
320 for NO_2 retrievals in Richter et al. (2011). Often only a few individual detector pixels are affected and in these
321 cases, it is possible to identify and remove the outliers from the fit. However, as the amplitude of the distortion
322 is usually only of the order of a few percent or less, it cannot always be found in the highly structured spectra
323 themselves. Higher sensitivity for spikes can be achieved by analysing the residual of the fit where the
324 contribution of the Fraunhofer lines, scattering, and absorption is already removed. When the residual for a
325 single pixel exceeds the average residual of all pixels by a chosen threshold ratio (the tolerance factor), the
326 pixel is excluded from the analysis, in an iterative process. This procedure is repeated until no further outliers
327 are identified, or until the maximum number of iterations is reached (here fixed to 3). Tests performed with
328 OMI spectra show that a tolerance factor of 5 improves the HCHO fits. This is especially important to handle
329 the sensitivity of 2-D detector arrays to high energy particles. However, this improvement of the algorithm has
330 a non-negligible impact on the time of processing (x 1.8). This option is activated in the QA4ECV algorithm,
331 and will be activated in the TROPOMI operational algorithm in the next update of the processor.

332 **2.2.2 Tropospheric air mass factor**

333 In the DOAS approach, an optically thin atmosphere is assumed. The mean optical path of scattered photons
334 can therefore be considered as independent of the wavelength within the relatively small spectral interval
335 selected for the fit. One can therefore define a single effective air mass factor given by the ratio of the slant to
336 the vertical optical depth of a particular absorber j:

$$M_j = \frac{\tau_{s,j}}{\tau_{v,j}}.$$ (6)

13

337 In the troposphere, scattering by air molecules, clouds and aerosols leads to complex light paths and therefore
338 complex altitude-dependent air mass factors. Full multiple scattering calculations are required for the
339 determination of the air mass factors, and the vertical distribution of the absorber has to be assumed *a priori*.
340 For optically thin absorbers, the formulation of Palmer et al. (2001) is conveniently used. It decouples the
341 height-dependent measurement sensitivity from the vertical profile shape of the species of interest, so that the
342 tropospheric AMF (M) can be expressed as the sum of the altitude dependent air mass factors (m_l) weighted
343 by the partial columns (n_{al}) of the a priori vertical profile in each vertical layer l, from the surface up to the
344 tropopause index (lt):

$$M = \frac{\sum_{l=1}^{l=lt} m_l(\lambda,\theta_0,\theta,\varphi,A_s,p_s,f_c,A_{cloud},p_{cloud})n_{al}(lat,long,time)}{\sum_{l=1}^{l=lt} n_{al}(lat,long,time)}, \qquad (7)$$
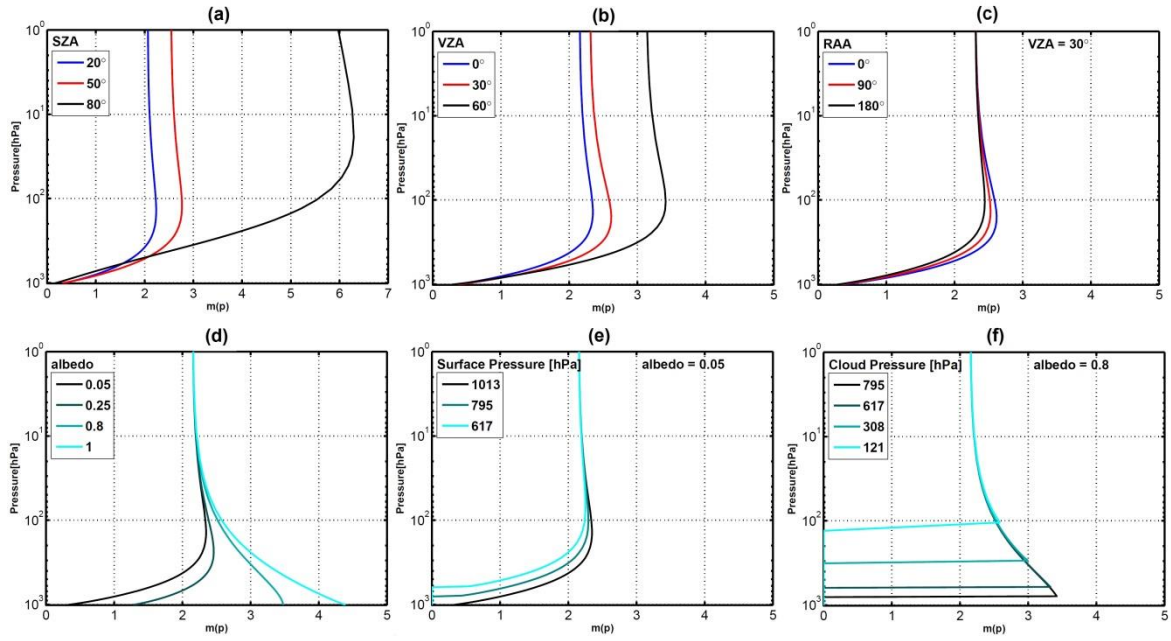
345 where A_s is the surface albedo, p_s is the surface pressure, and f_c, A_{cloud} and p_{cloud} are respectively the cloud
346 fraction, cloud albedo and cloud top pressure.

347 The altitude dependent air mass factors represent the sensitivity of the slant column to a change of the partial
348 columns $N_{v,j}$ at a certain level. In a scattering atmosphere, m_l depends on the wavelength, the viewing angles,
349 the surface albedo, and the surface pressure, but not on the partial column amounts or the vertical distribution
350 of the considered absorber (optically thin approximation).

351 **LUT of altitude dependent air mass factors**

352 Generally speaking, m depends on the wavelength, as scattering and absorption processes vary with
353 wavelength. However, in the case of HCHO, the amplitude of the M variation is found to be small (less than
354 5% for SZA lower than 70°) in the 328.5-346 nm fitting window and a single air mass factor representative for
355 the entire wavelength interval is used at 340 nm (Lorente et al., 2017).

356 Figure 6 illustrates the dependency of m with the observation angles, *i.e.* θ_0 (a), θ (b), and φ (c), and with scene
357 conditions like A$_s$ (d) and p_s for a weakly (e) or highly reflecting surface (f) (symbols in Table 4). The decrease
358 of sensitivity in the boundary layer is more important for large solar zenith angles and wide instrumental
359 viewing zenith angles. The relative azimuth angle does have relatively less impact on the measurement
360 sensitivity (note however that aerosols and BRDF effects are not included in those simulations). In the UV,
361 surfaces not covered with snow have an albedo lower than 0.1, while snow and clouds generally present larger
362 albedos. For a weakly reflecting surface, the sensitivity decreases near the ground because photons are mainly
363 scattered, and scattering can take place at varying altitudes. Larger values of the surface albedo increase the
364 fraction of reflected compared to scattered photons, increasing measurement sensitivity to tropospheric
365 absorbers near the surface. Over snow or ice also multiple scattering can play an important role further
366 increasing the sensitivity close to the surface.

367

Figure 6: Variation of the altitude dependent air mass factor with: (a) solar zenith angle, (b) viewing zenith angle, (c) relative azimuth angle between the sun and the satellite, (d) surface albedo, (e) surface pressure for a weakly reflecting surface, (f) surface pressure for a highly reflecting surface. Unless specified, the parameters chosen for the radiative transfer simulations are: SZA=30°, VZA=0°, RAA=0°, albedo=0.05, surface pressure=1063hPa, λ=340nm.

Altitude dependent air mass factors are calculated with the VLIDORT v2.6 radiative transfer model (Spurr, 2008), at 340 nm, using an US standard atmosphere, for a number of representative viewing geometries, surface albedos and surface pressures (used both for ground and cloud surface pressures), and stored in a look-up table. Altitude dependent air mass factors are then interpolated within the lookup table for each particular observation condition and interpolated vertically on the pressure grid of the a priori profile, defined within the TM5-MP model (Williams et al., 2017). Linear interpolations are performed in $\cos(\theta_0)$, $\cos(\theta)$, relative azimuth angle and surface albedo, while a nearest neighbour interpolation is performed in surface pressure. The parameter values chosen for the look-up table are detailed in Table 4. In particular, the grid of surface pressure is very thin near the ground, in order to minimise interpolation errors caused by the generally low albedo of ground surfaces. Indeed, as illustrated by Figure 6 (e) and (f), the variation of the altitude dependent air mass factors is more discontinuous with surface elevation (low reflectivity) than with cloud altitude (high reflectivity). Furthermore, the LUT and model pressures are scaled to their respective surface pressures, in order to avoid extrapolations outside the LUT range.

Table 4: Parameters in the altitude dependent air mass factors lookup table

Parameter name	Nb. of grid points	Grid of values	Symbol
Solar zenith angle [°]	17	0, 10, 20, 30, 40, 45, 50, 55, 60, 65, 70, 72, 74, 76, 78, 80, 85	θ_0
Line of sight zenith angle [°]	10	0, 10, 20, 30, 40, 50, 60, 65, 70, 75	θ

Relative azimuth angle [°]	5	0, 45, 90, 135, 180	φ
Surface albedo	14	0, 0.01, 0.025, 0.05, 0.075, 0.1, 0.15, 0.2, 0.25, 0.3 0.4, 0.6, 0.8, 1.0	A_s
Surface pressure [hPa]	17	1063.10, 1037.90, 1013.30, 989.28, 965.83, 920.58, 876.98, 834.99, 795.01, 701.21, 616.60, 540.48, 411.05, 308.00, 226.99, 165.79, 121.11	p_s
Atmospheric pressure [hPa]	64	1056.77, 1044.17, 1031.72, 1019.41, 1007.26, 995.25, 983.38, 971.66, 960.07, 948.62, 937.31, 926.14, 915.09, 904.18, 887.87, 866.35, 845.39, 824.87, 804.88, 785.15, 765.68, 746.70, 728.18, 710.12, 692.31, 674.73, 657.60, 640.90, 624.63, 608.58, 592.75, 577.34, 562.32, 547.70, 522.83, 488.67, 456.36, 425.80, 396.93, 369.66, 343.94, 319.68, 296.84, 275.34, 245.99, 210.49, 179.89, 153.74, 131.40, 104.80, 76.59, 55.98, 40.98, 30.08, 18.73, 8.86, 4.31, 2.18, 1.14, 0.51, 0.14, 0.03, 0.01, 0.001	p_l
Altitude corresponding to the atmospheric pressure, using an US standard atmosphere [km] (for information)	64	-0.35, -0.25, -0.15, -0.05, 0.05, 0.15, 0.25, 0.35, 0.45, 0.55, 0.65, 0.75, 0.85, 0.95, 1.10, 1.30, 1.50, 1.70, 1.90, 2.10, 2.30, 2.50, 2.70, 2.90, 3.10, 3.30, 3.50, 3.70, 3.90, 4.10, 4.30, 4.50, 4.70, 4.90, 5.25, 5.75, 6.25, 6.75, 7.25, 7.75, 8.25, 8.75, 9.25, 9.75, 10.50, 11.50, 12.50, 13.50, 14.50, 16.00, 18.00, 20.00, 22.00, 24.00, 27.50, 32.50, 37.50, 42.50, 47.50, 55.00, 65.00, 75.00, 85.00, 95.00	z_l

387 **Treatment of partly cloudy scenes**

388 The AMF calculations for TROPOMI will use the cloud fraction (f_c), cloud albedo (A_{cloud}) and cloud pressure

389 (p_{cloud}) from the S5P operational cloud retrieval, treating clouds as Lambertian reflectors (OCRA/ROCINN-

390 CRB, Loyola et al., 2017). The applied cloud correction is based on the independent pixel approximation

391 (Martin et al., 2002 and Boersma et al., 2004), in which an inhomogeneous satellite pixel is considered as a

392 linear combination of two independent homogeneous scenes, one completely clear and the other completely

393 cloudy. The intensity measured by the instrument for the entire scene is decomposed into the contributions

394 from the clear-sky and cloudy fractions. Accordingly, for each vertical layer, the altitude dependent air mass

395 factor of a partly cloudy scene is a combination of two air mass factors, calculated respectively for the cloud-

396 free and cloudy fractions of the scene:

$$m_l = (1 - w_c)m_{l\_clear}(A_s, p_s) + w_c m_{l\_cloud}(A_{cloud}, p_{cloud}) \tag{8}$$

397 where m_{l_clear} is the altitude dependent air mass factor for a completely cloud-free pixel, m_{l_cloud} is the altitude

398 dependent air mass factor for a completely cloudy scene, and the cloud radiance fraction w_c is defined as:

$$w_c = \frac{f_c I_{cloud}(A_{cloud}, p_{cloud})}{(1 - f_c)I_{clear}(A_s, p_s) + f_c I_{cloud}(A_{cloud}, p_{cloud})} \qquad (9)$$

399 I_{clear} and I_{cloud} are respectively the radiance intensities for clear-sky and cloudy scenes whose values are

400 calculated with VLIDORT at 340 nm and stored in look-up tables with the same grids as the altitude dependent

401 air mass factors. m_{l_clear} and I_{clear} are evaluated for a surface albedo A_s and a surface pressure p_s, while

402 m_{l_cloud} and I_{cloud} are estimated for a cloud albedo A_{cloud} and at the cloud pressure p_{cloud}. Note that the

403 variations of the cloud albedo are directly related to the cloud optical thickness. Strictly speaking in a

404 Lambertian (reflective) cloud model approach, only thick clouds can be represented (one should keep in mind

405 that still the penetration of photons into the cloud is not covered by the Lambertian model). An effective cloud

406 fraction corresponding to an effective cloud albedo of 0.8 ($f_{eff} = f_c \frac{A_c}{0.8}$) can be defined, in order to transform

407 optically thin clouds into equivalent optically thick clouds of reduced horizontal extent. In such altitude

408 dependent air mass factor calculations, a single cloud top pressure is assumed within a given viewing scene.

409 For low effective cloud fractions (f_{eff} lower than 10%), the cloud top pressure retrieval is generally highly

410 unstable and it is therefore reasonable to consider the observation as a clear-sky pixel (i.e. the cloud fraction is

411 set to 0) in order to avoid unnecessary error propagation through the retrievals. This 10% threshold might be

412 adjusted according to the quality of the cloud product (Veefkind et al., 2016; Loyola et al., 2017).

413 It should be noted that this formulation of the altitude dependent air mass factor for a partly cloudy pixel

414 implicitly includes a correction for the HCHO column lying below the cloud and therefore not seen by the

415 satellite, the so-called "ghost column". Indeed, the total AMF calculation as expressed by (7) and (8) assumes

416 the same a priori vertical profile in both cloudy and clear parts of the pixel and implies an integration of the

417 profile from the top of atmosphere to the ground, for each fraction of the scene. The ghost column information

418 is thus coming from the a priori profiles. For this reason, observations with cloud fractions f_{eff} larger than

419 30% are assigned with a poor quality flag and have to be used with caution.

420 **Aerosols**

421 The presence of aerosol in the observed scene may affect the quality of the retrieval. No explicit treatment of

422 aerosols (absorbing or not) is foreseen in the operational algorithm as there is no general and easy way to treat

423 the aerosols effect on the retrieval. At computing time, the aerosol parameters (extinction profile, single

424 scattering albedo, ...) are unknown. However, the information on the AAI (Stein Zweers et al., 2016) will be

425 included in the L2 HCHO files as it gives information to the user on the presence of absorbing aerosols and the

426 affected data should be used and interpreted with care.

427 **A priori vertical profile shapes**

428   Formaldehyde concentrations decrease with altitude as a result of the near-surface sources of short-lived
429   NMVOC precursors, the temperature dependence of CH_4 oxidation, and the altitude dependence of photolysis.
430   The profile shape varies according to local NMHC sources, boundary layer depth, photochemical activity, and
431   other factors.

432   To resolve this variability in the TROPOMI near-real time HCHO product, daily forecasts calculated with the
433   TM5-MP chemical transport model (Huijnen et al., 2010, Williams et al., 2017) will be used to specify the
434   vertical profile shape of the HCHO distribution. TM5-MP will also provide a priori profile shapes for the NO_2,
435   SO_2, and CO retrievals. For the QA4ECV OMI products, high-resolution TM5-MP model runs were performed
436   for the period 2004-2016, and the model profiles from this run are used for both HCHO and NO_2 retrievals.

437   TM5-MP is operated with a spatial resolution of 1°x1° in latitude and longitude, and with 34 sigma pressure
438   levels up to 0.1hPa in the vertical direction. TM5-MP uses 3-hourly meteorological fields from the European
439   Centre for Medium Range Weather Forecast (ECMWF) operational model (ERA-Interim reanalysis data for
440   reprocessing, and the operational archive for real time applications and forecasts). These fields include global
441   distributions of wind, temperature, surface pressure, humidity, and (liquid and ice) water content, and
442   precipitation.

443   For the calculation of the HCHO air mass factors, the profiles are linearly interpolated in space and time, at
444   pixel centre and local overpass time, through a model time step of 30 minutes. To reduce the errors associated
445   to topography and the lower spatial resolution of the model compared to the TROPOMI 3.5x7 km^2 spatial
446   resolution, the a priori profiles need to be rescaled to effective surface elevation of the satellite pixel. Following
447   Zhou et al. (2009) and Boersma et al (2011), the TM5-MP surface pressure is converted by applying the
448   hypsometric equation and the assumption that the temperature changes linearly with height:

$$p_s = p_{s,TM5}\left(\frac{T_{TM5}}{(T_{TM5} + \Gamma(z_{TM5} - z_s))}\right)^{-\frac{g}{R\Gamma}} \tag{10}$$

449   Where $p_{s,TM5}$ and T_{TM5} are the TM5-MP surface pressure and temperature, $\Gamma = 0.0065 Km^{-1}$ the lapse rate,
450   z_{TM5} the TM5-MP terrain height, and z_s surface elevation for the satellite ground pixel from a digital elevation
451   map at high resolution. $R=287\ J\ kg^{-1}\ K^{-1}$ is the gas constant for dry air, and $g = 9.8ms^{-2}$ the gravitational
452   acceleration.

453   The pressure levels for the a priori HCHO profiles are based on the improved surface pressure level p_s:
454    $p_l = a_l + b_l p_s$, a_l and b_l being the constants that effectively define the vertical coordinate (Table 13).

455   Yearly averaged OMI air mass factors obtained using prior information summarized in Table 5, in particular
456   TM5-MP HCHO profiles, are presented in Figure 7, in order to give an overview of the tropospheric AMF
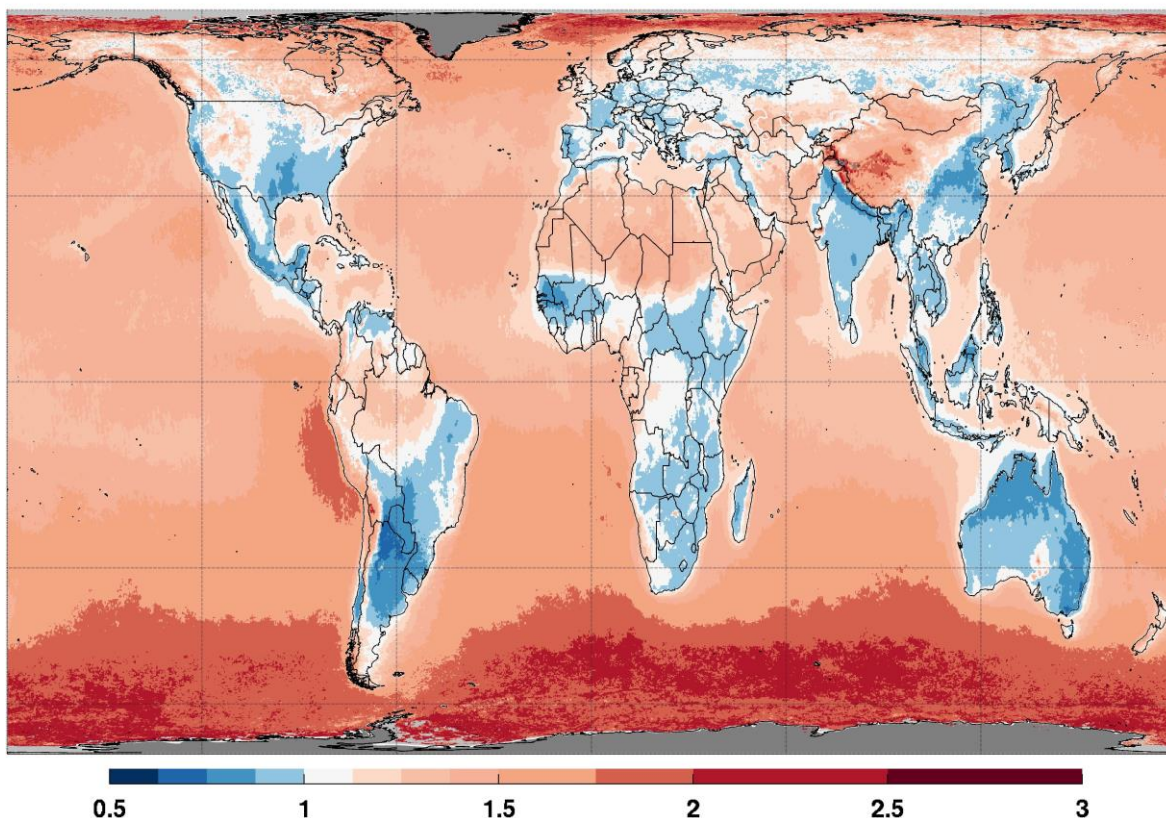457   values and their global regional variations.

Table 5: Prior information datasets used in the air mass factor calculation in the S5P HCHO operational algorithm and in the QA4ECV OMI algorithm.

Prior information	Origin of data set	Resolution	Symbol
Surface Albedo	OMI-based monthly minimum LER (update of Kleipool et al., 2008) When available, the TROPOMI-based LER product will be used.	• month • 0.5°x0.5° (lat x long) • 342 nm	A_s
Digital elevation map	GMTED2010 (Danielson et al., 2011)	Average over the ground pixel area.	z_s
Cloud fraction	Operational cloud product based on a Lambertian cloud model (S5P: Loyola et al., 2017; OMI: Veefkind et al., 2016).	For each ground pixel.	f_c
Cloud pressure			p_{cloud}
Cloud albedo			A_{cloud}
A priori HCHO profiles	Forecast (NRT) or reanalysis from TM5-MP CTM	• Daily profiles at overpass time • 1°x1° (lat x long) • 34 sigma pressure levels up to 0.1hPa	n_a

Figure 7: Yearly averaged map of tropospheric air mass factors at 340 nm using the QA4ECV OMI HCHO algorithm. A priori HCHO profiles from high-resolution TM5-MP model runs have been used. The IPA cloud correction is applied for effective cloud fractions f_{eff} larger than 10%. Observations with f_{eff} larger than 30% have been filtered out.

2.2.3 Across-track and zonal reference sector correction

Residual latitude-dependent biases in the columns, due to unresolved spectral interferences, are known to remain a limiting factor for the retrieval of weak absorbers such as HCHO. Retrieved HCHO slant columns can present large offsets depending on minor changes in the fit settings, and on minor instrumental spectral inaccuracies. Resulting offsets are generally global but also show particular dependencies, mainly with detector row (across-track) and with latitude (along-track). In the case of a 2D-detector array such as OMI or TROPOMI, across-track striping can possibly arise, due to imperfect calibration and different dead/hot pixel masks for the CCD detector regions. Offset corrections are also meant to handle some effects of the time-dependent degradation of the instrument.
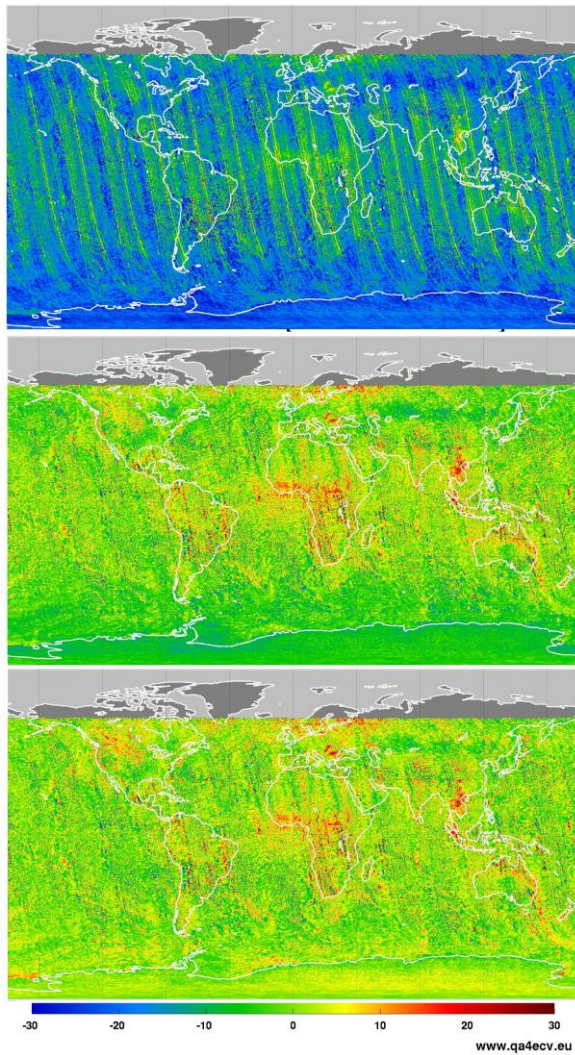
A large part of the resulting systematic HCHO slant column uncertainty is reduced by the application of a background correction, which is based on the assumption that the background HCHO column observed over remote oceanic regions (Pacific Ocean) is only due to methane oxidation. The natural background level of HCHO is well estimated from chemistry model simulations of CH_4 oxidation ($N_{v,0,CTM}$). It is ranging from 2 to $4x10^{15}$ molec.cm^{-2}, depending on the latitude and the season (De Smedt et al., 2008; 2015; González Abad et al., 2015).

For the HCHO retrieval algorithm, we use a 2-steps normalization of the slant columns (see Figure 8 and Table 6):

- Across-track: the mean HCHO slant column is determined for each row in the reference sector around the equator [-5° 5°], [180° 240°]. Data selection is based on the slant column errors from the DOAS fit and on the cloud fraction (threshold values are given in Table 6). Those mean HCHO values are subtracted from all the slant columns of the same day, as a function of the row. The aim is to reduce possible row-dependent offsets. In the case were solar irradiance are used as reference, those offsets can exceed $2x10^{16}$ molec.cm^{-2} (see the first panel of Figure 8). They are reduced below 10^{15} molec.cm^{-2} by this first step, or when row averaged radiances are used as reference, as in the QA4ECV algorithm (middle panel of Figure 8).
- Along-track: the latitudinal dependency of the across-track corrected HCHO SCs is modelled by a polynomial fit through their mean values, all rows combined, in 5° latitude bins in the reference sector ([-90° 90°], [180° 240°]). Again, data selection is based on the slant column errors from the DOAS fit and on the cloud fraction.

These two corrections are applied to the global slant columns so that in the reference sector, the mean background corrected slant columns ($\Delta N_s = N_s - N_{s,0}$) are centered around zero (lower panel of Figure 8).

02 Feb. 2005   OMI HCHO Ns [x10^{15} molec.cm^{-2}]

496

497   **Figure 8: Illustration of the across-track and zonal reference sector correction steps applied to one day**
498   **of OMI HCHO slant columns (02/02/2005). The upper panel shows the uncorrected slant columns**
499   **obtained using as DOAS reference spectrum the solar irradiance. The center panel shows the same**
500   **slant columns after the first across-track correction step or when row averaged radiances selected in**
501   **the Pacific Ocean are used as reference. The lower panel shows the final background corrected slant**
502   **columns ΔN_s.**

503   **Table 6: 2-steps normalization of the HCHO vertical columns**

Correction	Region	Time frame	Column correction	Observation selection
Across-track	Equatorial Pacific Lat: [-5° 5°], Long: [180° 240°]	NRT: 1-week moving window	$dN_s(\text{row}) = N_s(\text{row}) - \overline{N_{s,0}}(\text{row})$	$\sigma_{N_s} \leq 3\overline{\sigma_{N_s}}$ $f_c \leq 0.4$
Zonal Along-track	Pacific Lat: [-90° 90°], Long: [180° 240°]	Offline: Daily correction	$\Delta N_s(lat) = dN_s(lat) - \overline{dN_{s,0}}(lat)$ $\overline{N_{s,0,CTM}}(lat) = \overline{M_0}(lat)\overline{N_{v,0,CTM}}(lat)$	$\overline{dN_{s,0}}(lat) \leq 5e16$

504 To the corrected slant columns, the background HCHO values from a model have to be added. A latitude-
505 dependent polynomial is fitted daily through 5° latitude bin means of those modelled values in the reference
506 sector. Corresponding values are added to all the columns of the day. Strictly speaking, those background
507 values should be slant columns, derived as the product of air mass factors in the reference sector (M_0) with
508 HCHO vertical columns from the model ($N_{s,0,CTM} = M_0 N_{v,0,CTM}$) (González Abad et al., 2015). However, this
509 option requires the storage of the slant columns, the air mass factors, and their errors, in a separated database
510 (QA4ECV Algorithm and S5P option, see Equation (11)). An approximate solution is to add as background
511 the constant vertical column from the model ($N_{v,0,CTM}$), hence neglecting the variability of the *M_0/M* ratio. This
512 is the current implementation in the S5P algorithm, which will be updated with equation (11) after launch. For
513 NRT purpose, the evaluation in the reference sector is made using a moving time window of 1 week. For offline
514 processing, the reference sector correction can be refined by using daily evaluations.

$$N_v = \frac{N_s - N_{s,0}}{M} + N_{v,0} = \frac{\Delta N_s}{M} + \frac{M_0}{M} N_{v,0,CTM} = \frac{\Delta N_s + N_{s,0,CTM}}{M} \tag{11}$$

515 Figure 3 presents some examples of monthly and regionally averaged vertical columns, together with the
516 contribution of $N_{v,0}$. It should be realized that this contribution accounts for 20 to 50% of the vertical columns,
517 as expected from the large contribution of methane oxidation to the total HCHO column (Stavrakou et al.,
518 2015).

519 **3. Uncertainty analyses**

520 **3.1 Uncertainty formulation by uncertainty propagation**

521 The total uncertainty on the HCHO vertical column is composed of many sources of (random and systematic)
522 errors. In part those are related to the measuring instrument, such as errors due to noise or knowledge of the
523 slit function. In a DOAS-type algorithm, those instrumental errors propagate into the uncertainty of the slant
524 columns. Other types of error can be considered as model errors and are related to the representation of the
525 observation physical properties that are not measured. Examples of model errors are errors on the trace gas
526 absorption cross-sections, the treatment of clouds and errors of the a priori profiles. Model errors can affect the
527 slant columns, the air mass factors or the applied background corrections.

528 A formulation of the uncertainty can be derived analytically by uncertainty propagation, starting from the

equation of the vertical column (11) which directly results from the different retrieval steps. As the main algorithm steps are performed independently, they are assumed to be uncorrelated. The total uncertainty on the tropospheric vertical column can be expressed as (Boersma et al., 2004, De Smedt et al., 2008):

$$\sigma_{N,v}{}^2 = \left(\frac{\partial N_v}{\partial N_s}\sigma_{N,s}\right)^2 + \left(\frac{\partial N_v}{\partial M}\sigma_M\right)^2 + \left(\frac{\partial N_v}{\partial N_{s,0}}\sigma_{N,s,0}\right)^2 + \left(\frac{\partial N_v}{\partial M_0}\sigma_{M,0}\right)^2$$
$$+ \left(\frac{\partial N_v}{\partial N_{v,0,CTM}}\sigma_{N,v,0,CTM}\right)^2 \tag{12}$$

$$\sigma_{N,v}{}^2 = \frac{1}{M^2}\left(\sigma_{N,s}{}^2 + \frac{(\Delta N_S + M_0 N_{v,0,CTM})^2}{M^2}\sigma_M{}^2 + \sigma_{N,s,0}{}^2 + N_{v,0,CTM}{}^2\sigma_{M,0}{}^2\right. \tag{13}$$
$$\left. + M_0{}^2\sigma_{N,v,0,CTM}{}^2\right)$$

where $\sigma_{N,s}$, σ_M, $\sigma_{N,s,0}$, $\sigma_{M,0}$ and $\sigma_{N,v,0,CTM}$ are respectively the uncertainties on the slant column, the air mass factor, and the slant column correction, the air mass factor, and the model vertical column in the reference sector (indicated by suffix 0). For each of these categories, the following sections provide more details on the implementation of the uncertainty estimate in the HCHO algorithm. A discussion of the sources of uncertainties and, where possible, their estimated size are presented, as well as their spatial and temporal patterns.

Note that in the current implementation of the operational processor, $M_0 = M$, and the uncertainty formulation therefore reduces to:

$$\sigma_{N,v}{}^2 = \frac{1}{M^2}\left(\sigma_{N,s}{}^2 + \frac{\Delta N_S{}^2}{M^2}\sigma_M{}^2 + \sigma_{N,s,0}{}^2\right) + \sigma_{N,v,0,CTM}{}^2 \tag{14}$$

Complementing this uncertainty propagation analysis, total column averaging kernels (*A*) based on the formulation of Eskes and Boersma (2003) are estimated. Column averaging kernels provide essential information when comparing measured columns with e.g. model simulations or correlative validation data sets, because they allow removing the effect of the a-priori HCHO profile shape used in the retrieval (see APPENDIX C: Averaging Kernel, Boersma et al., 2004; 2016).

Section 3.2 presents our current estimates of the precision (random uncertainty) and the trueness (systematic uncertainty) that can be expected for the TROPOMI HCHO vertical columns. They are discussed along with the product requirements (Section 2.1).

3.1.1 Errors on the slant columns

Error sources that contribute to the total uncertainty on the slant column originate both from instrument characteristics and from errors in the DOAS slant column fitting procedure itself.

The retrieval noise for individual observations is limited by the SNR of the spectrometer measurements. A good estimate of the random variance of the reflectance (which results from the combined noise of radiance

and reference spectra) is given by the reduced χ^2 of the fit, which is defined as the sum of squares (4) divided by the number of degrees of freedom in the fit. The covariance matrix (Σ) of the linear least squares parameter estimate is then given by:

$$\Sigma = \frac{\chi^2}{(k-n)}(A^T A)^{-1} \tag{15}$$

where k is the number of spectral pixels in the fitting interval, n is the number of parameters to fit and the matrix $A(j \text{ x } k)$ is formed by the cross-sections. For each absorber j, the value $\sigma_{N,s,j}$ is usually called the slant column error (SCE or $\sigma_{N,s,rand}$).

$$\sigma_{N,s,j}^2 = \frac{\chi^2}{(k-n)}(A^T A)_{j,j}^{-1} \tag{16}$$

Equation (16) does not take into account systematic errors, that are mainly dominated by slit function and wavelength calibration uncertainties, absorption cross-section uncertainties, by interferences with other species (O_3, BrO or O_4), or by uncorrected stray light effects. The choice of the retrieval interval can have a significant impact on the retrieved HCHO slant columns. The systematic contributions to the slant column errors are empirically estimated from sensitivity tests (see Table 7) and can be viewed as part of the structural uncertainty (Lorente et al., 2017). However, remaining systematic offsets and zonal biases are greatly reduced by the reference sector correction. All effects summed in quadrature, the various contributions are estimated to account for an additional systematic uncertainty of 20% of the background-corrected slant column:

$$\sigma_{N,s,syst} = 0.2 \Delta N_s \tag{17}$$

The total uncertainty on slant columns is then:

$${\sigma_{N,s}}^2 = {\sigma_{N,s,rand}}^2 + {\sigma_{N,s,syst}}^2 \tag{18}$$

Table 7: Summary of the different error sources considered in the HCHO slant column uncertainty budget.

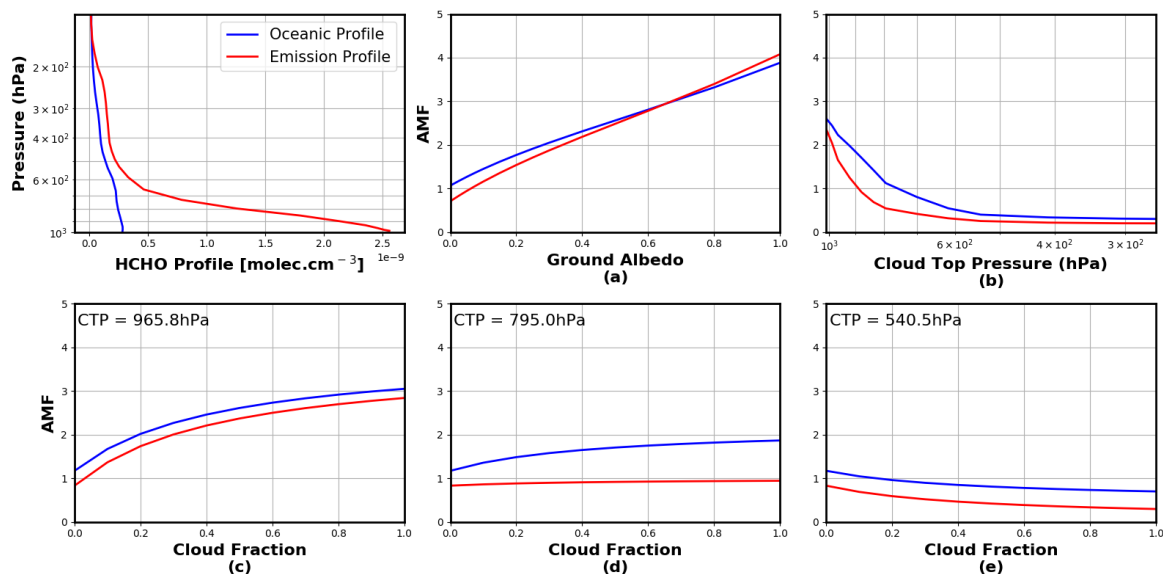| Error source	Parameter uncertainty	Estimated uncertainty on HCHO SCD	Evaluation method - reference
Measurement noise	S/N=800-1000	1×10^{16} molec.cm^{-2} (random)	Value derived for individual observations by uncertainty propagation; De Smedt et al., 2015;
HCHO cross-section error	Based on alternative cross-section datasets, offset and polynomial orders.	9%	Mean values derived from sensitivity tests using GOME-2 and OMI data.
O$_3$ cross-section error		5%	
BrO cross-section error		5%	De Smedt et al., 2008; 2015
NO$_2$ cross-section error		3%	Hewson et al., 2013
O$_4$ cross-section error		2%	Pinardi et al., 2013
Ring correction error		5%	
Choice of offset order		7%	

Choice of polynomial order		7%	
Instrumental slit function and wavelength calibration	Based on alternative calibrations	10%	Mean value derived from sensitivity tests using GOME-2 and OMI data.
Choice of wavelength interval	Based on alternative wavelength intervals	10%	Mean value derived from sensitivity tests using GOME-2 and OMI data. Hewson et al., 2013
Temperature dependence of the HCHO XS	0.05%/°K	2%	Mean value derived from sensitivity tests based on Meller and Moorgat (2000)

3.1.2 Errors on air mass factors

The uncertainties on the air mass factor depend on input parameter uncertainties and on the sensitivity of the air mass factor to each of them. This contribution is broken down into the squared sum (Boersma et al., 2004, De Smedt et al., 2008):

$$\sigma_M{}^2 = \left(\frac{\partial M}{\partial A_s} \cdot \sigma_{A,s}\right)^2 + \left(\frac{\partial M}{\partial f_c} \cdot \sigma_{f,c}\right)^2 + \left(\frac{\partial M}{\partial p_{cloud}} \cdot \sigma_{p,cloud}\right)^2 + \left(\frac{\partial M}{\partial s} \cdot \sigma_s\right)^2 + (0.2M)^2 \qquad (19)$$

The contribution of each parameter to the total air mass factor error depends on the observation conditions. The air mass factor sensitivities ($M' = \frac{\partial M}{\partial parameter}$), i.e. the air mass factor derivatives with respect to the different input parameters, can be derived for any particular condition of observation using the altitude-dependent AMF LUT, and using the model profile shapes (see Figure 9). In practice, a LUT of AMF sensitivities has been created using coarser grids than the AMF LUT, and one parameter describing the shape of the profile: the profile height, i.e. the altitude (pressure) below which resides 75% of the integrated HCHO profile. $\frac{\partial M}{\partial s}$ is approached by $\frac{\partial M}{\partial s_h}$ where s_h is half of the profile height. Relatively small variations of this parameter have a strong impact on the total air mass factors, because altitude-resolved air mass factors decrease quickly in the lower troposphere, where the HCHO profiles peak (Figure 6).

Figure 9: First panel: TM5-MP HCHO profiles extracted in June over the equatorial Pacific ocean (blue) and over Beijing (red). Those profiles have been used to calculated the tropospheric air mass factors shown in the panels a to e, representing the AMF dependence on (a) the surface albedo, (b) the cloud altitude, (c), (d), (e) the cloud fraction. In all cases, we consider a nadir view and a solar zenith angle of 30°. In (a) the pixel is cloud free, in (b) the albedo is 0.02 and the effective cloud fraction is 0.5, in (c), (d), (e) the ground albedo is 0.02 and the cloud pressure is respectively 966, 795 and 540 hPa.
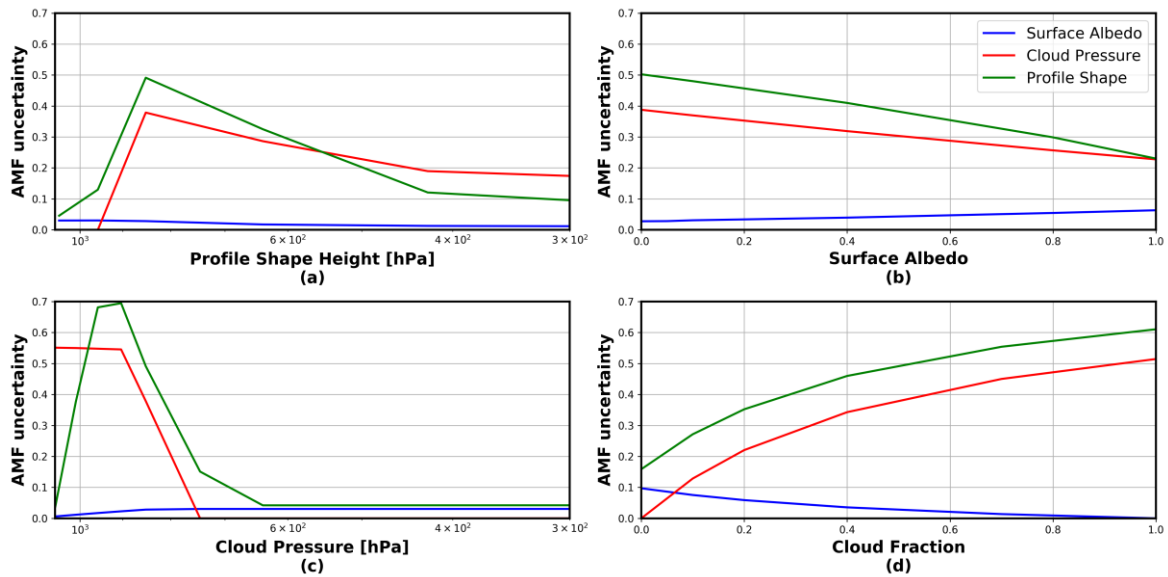
The uncertainties $\sigma_{A,s}, \sigma_{f,c}, \sigma_{p,cloud}, \sigma_{s,h}$ are typical uncertainties on the surface albedo, cloud fraction, cloud top pressure and profile shape, respectively. They are estimated from the literature or derived from comparisons with independent data (see Table 8). Together with the sensitivity coefficients, these give the first four contributions on the right of equation (19). The fifth term on the right of equation (19) represents the uncertainty contribution due to possible errors in the AMF model itself (Lorente et al., 2017). We estimate this contribution to 20% of the air mass factor (see also section 3.2.2).

Estimates of the air mass factor uncertainties and of their impact on the vertical column uncertainties are listed in Table 8 and represented in Figure 10. They are based on the application of equation (19) to HCHO columns retrieved from OMI measurements. In expression (19), the impact of possible correlations between errors on parameters is not considered, like for example the surface albedo and the cloud top pressure. Note also that errors on the solar angles, the viewing angles and the surface pressure are supposed to be negligible, which is not totally true in practice, since equation (10) does not yield the true surface pressure but only a good approximation.

602 **Table 8: Summary of the different error sources considered in the air mass factor uncertainty budget.**

Input parameter error	Symbol	Parameter Uncertainty	Source	Estimated uncertainty on HCHO VCD
Surface albedo	σ_{A_s}	0.02	Kleipool et al., 2008	10-20%
Cloud fraction	$\sigma_{f,c}$	0.05	Veefkind et al., 2016	05-15%
Cloud height	$\sigma_{p,cloud}$	50hPa		10-20%
Profile shape height	σ_s	75hPa	Upper limit of TM5-MP profile height standard deviation.	20-60%
AMF wavelength dependency	Model / Structural uncertainty	20%	Lorente et al., 2017	15-35%
LUT interp. errors				
Model atmosphere				
Cloud model/cloud correction/				
No explicit aerosol correction				

603

604

605 **Figure 10: AMF uncertainty related to profile shape, cloud pressure and surface albedo errors, as a**
606 **function of different observation conditions. In all cases, we consider a nadir viewing and a solar zenith**
607 **angle of 30°. By default, fixed values have been used. The surface pressure is 1063hPa, the albedo is 0.05,**
608 **the effective cloud fraction is 0.5, and the profile height and cloud pressure are 795 hPa.**

609

610 **Surface albedo**

611 A reasonable uncertainty on the albedo is 0.02 (Kleipool et al., 2008). This translates to an uncertainty on the
612 air mass factor using the slope of the air mass factor as a function of the albedo and can be evaluated for each

27

satellite pixel (equation (19)). As an illustration, Figure 9 (a) shows the air mass factor dependence on the ground albedo for two typical HCHO profile shapes (in blue: remote profile, in red: emission profile). At 340nm, the AMF sensitivity (the slope), is almost constant with albedo, being only slightly higher for low albedo values. As expected, the AMF sensitivity to albedo is higher for an emission profile peaking near the surface than for a background profile more spread in altitude. More substantial errors can be introduced if the real albedo differs considerably from what is expected, for example in the case of the sudden snowfall or ice cover. Snow/ice cover map will therefore be used for flagging such cases.

Clouds and aerosols

An uncertainty on the cloud fraction of 0.05 is considered, while an uncertainty on the cloud top pressure of 50hPa is taken. Figure 9 (b) shows the air mass factor variation with cloud altitude. The AMF is very sensitive to the cloud top pressure (the slope is steepest) when the cloud is located below or at the level of the formaldehyde peak. For higher clouds, the sensitivity of the air mass factor to any change in cloud pressure is very weak. As illustrated in Figure 9 (c), (d) and (e), for which a cloud top pressure of 966, 795 and 540 hPa is respectively considered, the sensitivity to the cloud fraction is mostly significant when the cloud lies below the HCHO layer.

The effect of aerosols on the air mass factors are not explicitly considered in the HCHO retrieval algorithm. To a large extent, however, the effect of the non-absorbing part of the aerosol extinction is implicitly included in the cloud correction (Boersma et al., 2011). Indeed, in the presence of aerosols, the cloud detection algorithm is expected to overestimate the cloud fraction. Since non-absorbing aerosols and clouds have similar effects on the radiation in the UV-visible range, the omission of aerosols is partly compensated by the overestimation of the cloud fraction, and the resulting error on air mass factor is small, typically below 15% (Millet et al., 2006; Boersma et al., 2011; Lin et al., 2014; Castellanos et al., 2015; Chimot et al. 2015). In some cases, however, the effect of clouds and aerosols will be different. For example, when the cloud height is significantly above the aerosol layer, clouds will have a shielding effect while the aerosol amplifies the signal through multiple scattering. This will result in an underestimation of the AMF. Absorbing aerosols have also a different effect on the air mass factors, since they tend to decrease the sensitivity to HCHO concentration. In this case, the resulting error on the air mass factor can be as high as 30% (Palmer et al., 2001; Martin et al., 2002). This may, for example, affect significantly the derivation of HCHO columns in regions dominated by biomass burning as well as over heavily industrialized regions. Shielding and reflecting effect can thus occur, depending on the observation, decreasing or increasing the sensitivity to trace gas absorption. It has been shown that uncertainties related to aerosols is reduced by spatiotemporal averaging (Barkley et al., 2012; Lin et al., 2014; Castellanos et al., 2015; Chimot et al. 2015). Furthermore, the applied cloud filtering effectively removes observations with the largest aerosol optical depth. In the HCHO product, observations with an elevated absorbing aerosol index will be flagged, to be used with caution.

Profile shape

649 This contribution to the total AMF error is the largest when considering monthly averaged observations. This
650 is supported by validation results using MAX-DOAS profiles measured around Beijing and Wuxi (see De
651 Smedt et al. 2015, Wang et al., 2016). Taking into account the averaging kernels allows removing from the
652 comparison the error related to the a priori profiles, when validating the results against other modelled or
653 measured profiles (see the APPENDIX C: Averaging Kernel).

3.1.3 Errors on the reference sector correction
654

655

$$\sigma_{N,v,0}{}^2 = \frac{1}{M^2}\left(\sigma_{N,s,0}{}^2 + N_{v,0,CTM}{}^2\sigma_{M,0}{}^2 + M_0{}^2\sigma_{N,v,0,CTM}{}^2\right) \tag{20}$$

656 This uncertainty includes contributions from the model background vertical column (see the recent study of
657 Anderson et al., 2017), from the error on the air mass factor in the reference sector, and from the amplitude of
658 the normalization applied to the HCHO columns. As mentioned in 3.1.1, we consider that $\sigma_{N,s,0}$ is taken into
659 account in Equation (17). The uncertainty on the air mass factor in the reference sector $\sigma_{M,0}$ is calculated as in
660 Equation (19) and saved during the background correction step. Uncertainty on the model background has been
661 estimated as the absolute values of the monthly averaged differences between two different CTM simulations
662 in the reference sector: IMAGES (Stavrakou et al., 2009a) and TM5-MP (Huijnen et al., 2010). The differences
663 range between 0.5 and 1.5x10^{15} molec.cm^{-2}.

664 **Table 9: Estimated errors on the reference sector correction.**

Error source	Uncertainty on HCHO VCD	Evaluation method – reference
Model background	0.5 to 1.5x10^{15} molec.cm^{-2}	Difference between IMAGES and TM model
Amplitude of the column normalisation ($N_{s,0}$)	0 to 4x10^{15} molec.cm^{-2}	Sensitivity tests using GOME-2 and OMI data.

3.2 HCHO error estimates and product requirements

665

666 This section presents estimates of the precision (random error) and trueness (systematic error) that can be
667 expected for the TROPOMI HCHO vertical columns. These estimates are given in different NMVOC emission
668 regions. Precision and trueness of the HCHO product are discussed against the user requirements.
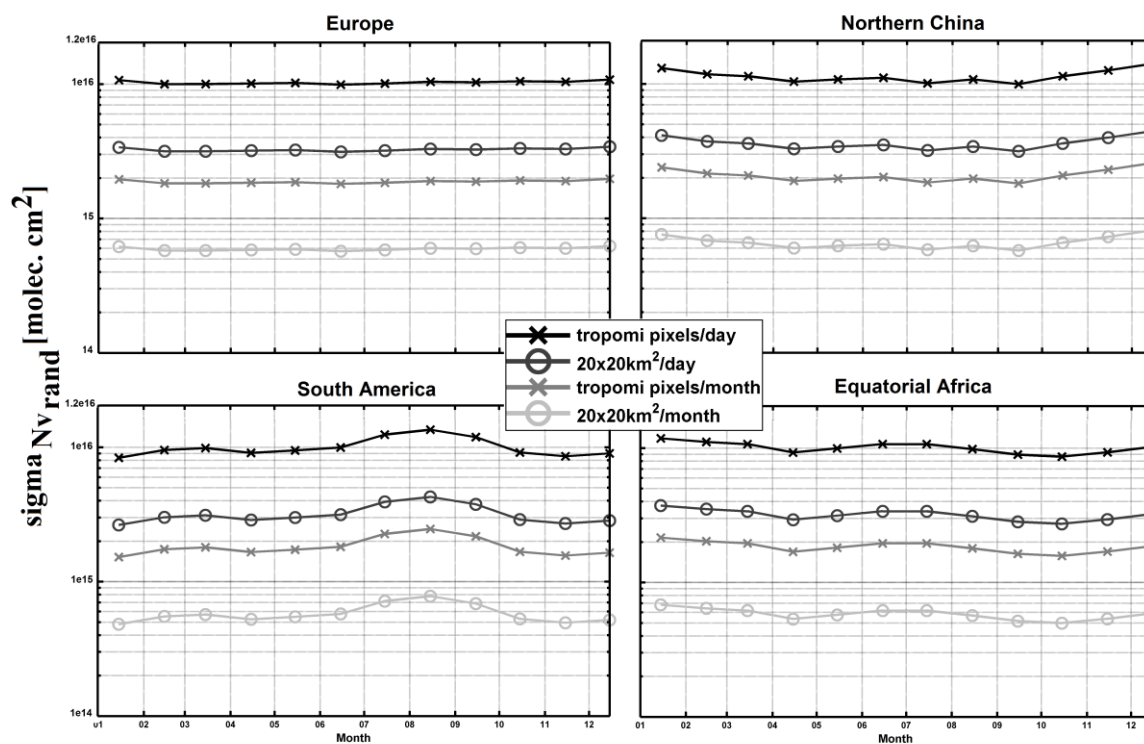
3.2.1 Precision
669

670 When considering individual pixels, the total uncertainty is dominated by the random error on the slant
671 columns. Our simulations and tests on real satellite measurements show that the precision by which the HCHO
672 can be measured is well defined by the instrument signal-to-noise level. For the nominal SNR level (1000), the
673 expected precision of single-pixel measurements is equivalent to the precision obtained with OMI HCHO
674 retrievals (De Smedt et al., 2015), but with a ground pixel size of about 3.5x7 km², i.e. one order of magnitude
675 smaller in surface. Absolute $\sigma_{N,s,rand}$ values typically range between 7 and 12x10^{15} molec.cm^{-2} for individual
676 pixels, showing an increase as a function of the surface altitude and of the solar zenith angle. Relative values
677 range between 100 and 300%, depending on the observation scene. In the case of HCHO retrievals, for
678 individual satellite ground pixels, the random error on the slant columns is the most important source of

679 uncertainty on the total vertical column. It can be reduced by averaging the observations, but of course at the

680 expense of a loss in time and/or spatial resolution.

681 The precision of the vertical columns provided in the L2 files corresponds to the precision of the slant column

682 divided by the air mass factor

683 $\sigma_{N,v,rand} = \frac{\sigma_{N,s,rand}}{M}$ (see Table 13). It is dependent on the air mass factors, and therefore on the observation

684 conditions and on the cloud statistics. Figure 11 shows the vertical column precision that is expected for

685 TROPOMI, based on OMI observations in 2005. Results are shown in several regions, and at different spatial

686 and temporal scales (from individual pixels to monthly averaged column in 20x20km² grids). The product

687 requirements for HCHO measurements state a precision of 1.3×10^{15} molec.cm^{-2}. This particular requirement

688 cannot be achieved with individual observations at full spatial resolution. However, as represented in Figure

689 11, the requirement can be approached using daily observations at the spatial resolution of 20x20km^2 (close to

690 the OMI resolution) or using monthly averaged columns at the TROPOMI resolution. The precision can be

691 brought below 1×10^{15} molec.cm^{-2} if a spatial resolution of 20x20km^2 is considered for monthly averaged
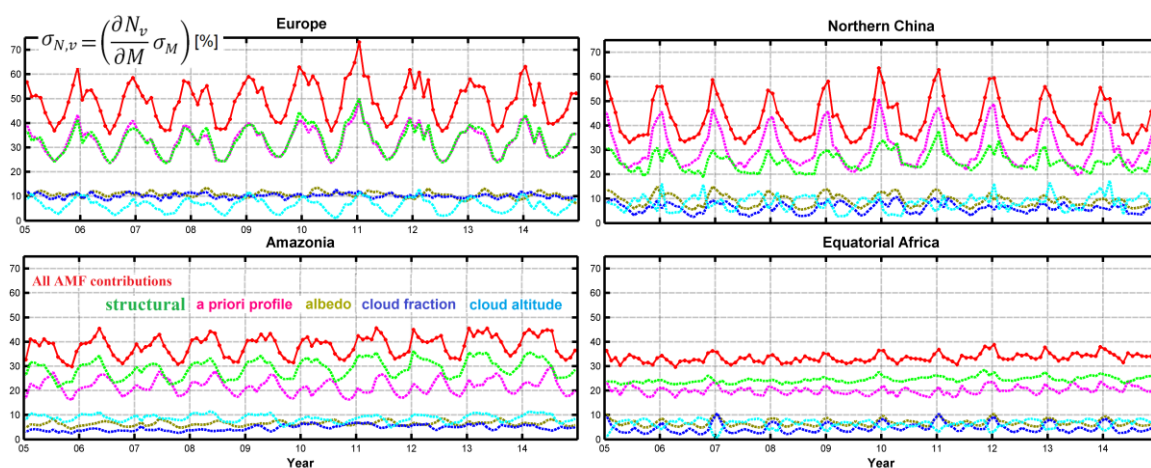
692 columns.

693

694 **Figure 11: Estimated precision on the TROPOMI HCHO columns, in several NMVOC emission**
695 **regions, and at different spatial and temporal scales (from individual pixels to monthly averages in**
696 **20x20 km² grids). These estimated are based on OMI observations in 2005, using observations with an**
697 **effective cloud fraction lower than 40%.**

698 **3.2.2 Trueness**

699 In this section, we present monthly averaged values of the systematic vertical columns uncertainties estimated

700 for OMI retrievals between 2005 and 2014. The contribution of the air mass factor uncertainties is the largest

701 contribution to the vertical column systematic uncertainties (see also Table 10). Figure 12 presents the VCD

702 uncertainties due to AMF errors, and the five considered contributions, over Equatorial Africa and Northern

703 China, as example of Tropical and mid-latitude sites. The largest contributions are from the a priori profile

704 uncertainty and from the structural uncertainty (taken as 20% of the AMF). In the case where the satellite

705 averaging kernels are used for comparisons with external HCHO columns, the a priori profile contribution can

706 be removed from the comparison uncertainty budget, leading to a total uncertainty in the range of 25% to 50%.

707 Table 10 wraps up the estimated relative contributions to the HCHO vertical column uncertainty, in the case

708 of monthly averaged columns for typical low and high columns.

709 Considering these estimates of the HCHO column trueness, the requirements for HCHO product (30%) are

710 achievable in regions of high emissions and for certain times of the year. In any case, observations need to be

711 averaged to reduce random uncertainties at a level comparable or smaller than systematic uncertainties.

712

Figure 12: Regional and monthly average of the relative systematic vertical column AMF-related uncertainties in several NMVOC emission regions, for the period 2005-2014. The 5 contributions to the systematic air mass factor uncertainty are shown: structural (green), a priori profile (pink), albedo (olive), cloud fraction (blue) and cloud altitude (cyan).

Table 10: Estimated HCHO vertical column uncertainty budget for monthly averaged low and elevated columns (higher than 1×10^{16} molec.cm^{-2}). Contributions from the three retrieval steps are provided, as well as input parameter contributions.

HCHO vertical error uncertainty	Remote regions / low columns	Elevated column regions / periods
Contribution from systematic slant columns uncertainties	25%	15%
Contribution from air mass factors uncertainties	75%	30%
• from a priori profile errors	• 60%	• 20%
• from model errors	• 35%	• 15%
• from albedo errors	• 20%	• 10%
• from cloud top pressure errors	• 20%	• 10%
• from cloud fraction errors	• 15%	• 05%
Contribution from background correction uncertainties	40%	10%
Total	**90%**	**35%**
Total without smoothing error	**50%**	**25%**

720

4. Verification

In the framework of the TROPOMI L2 WG and QA4ECV projects, extensive comparisons of the prototype (this paper), the verification (IUP-UB), and alternative scientific algorithms (MPIC, KNMI, WUR) have been conducted. All follow a common DOAS approach. Prototype and verification algorithms have been applied to both synthetic and OMI spectra. Here, we present a selection of OMI results. For a complete description of the verification algorithm as well as results and discussion of the retrievals applied to synthetic spectra, please refer to the TROPOMI verification report (Richter et al., 2015).

4.1 Harmonized DOAS fit settings using OMI test data
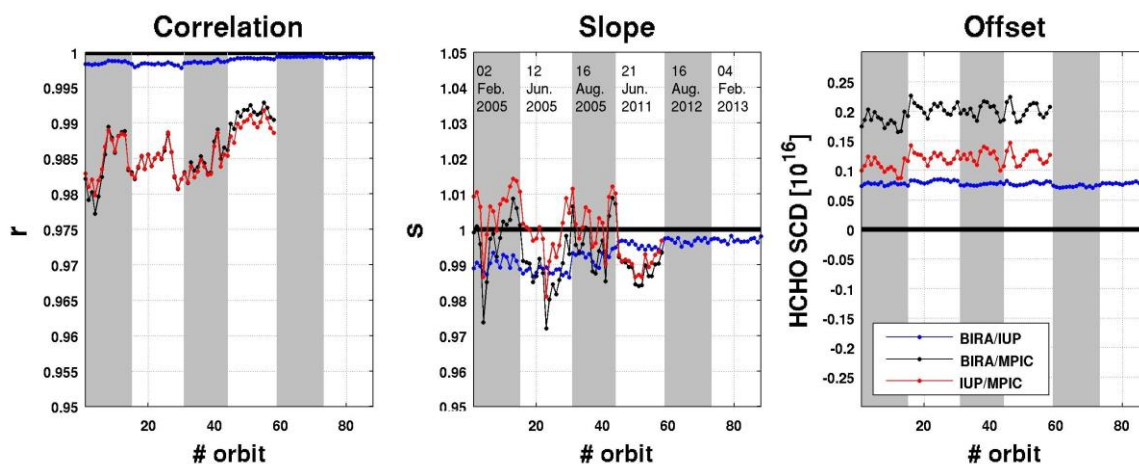
For this exercise, a common set of DOAS fit parameters has been agreed upon. The goal of the intercomparison of harmonized fit settings was to ensure that the software implementation of the different algorithms behaves as expected in a large range of realistic measurement scenarios. Another objective was to gain knowledge on the level of agreement/disagreement of results from different groups when using the same settings, as well as on the main drivers for differences. Common and simple fit parameters based on the operational and verification algorithm were selected. They are summarized in Table 11.

Table 11: Common DOAS fit settings for HCHO using OMI data.

Parameter	Values
Fitting interval-1	328.5-359 nm
Calibration	1 interval (328-359 nm), using the SAO 2010 solar atlas (Chance and Kurucz, 2010).
Molecular species	HCHO, NO_2, Ozone, BrO, O_2-O_2 : same cross-sections as in Table 4
Ring effect	Ring cross-section based on the technique outlined by Chance et al. (1997)
Slit function	One slit function per binned spectrum as a function of wavelength (60 OMI ISRF, Dirksen et al., 2006).
Polynomial	5th order
Intensity offset correction	Linear offset ($1/I_0$)
Reference spectrum I_0	Daily solar irradiance

The intercomparison of results using common settings allowed to identify and fix several issues in the different codes leading to an overall consolidation of the algorithms. It has been found that minor changes in the fit settings may lead to large offsets ($\pm 10 \times 10^{15}$ molec.cm^{-2}) in the HCHO SCDs. However, an excellent level of agreement ($\pm 2 \times 10^{15}$ molec.cm^{-2}) between the different retrieval codes was obtained after several iterations of the common settings. The main sources of discrepancies were found to be related to (1) the solar I_0 correction applied on the O_3 cross-sections, (2) the intensity offset correction, (3) the details of the wavelength calibration of the radiance and irradiance spectra, and (4) the OMI slit functions and their implementation in the convolution tools (Boersma et al., 2015).

745 An overview of the final SCD comparison is shown on Figure 13 for six test days at the beginning and the end

746 of the OMI time series, and for a particular OMI orbit on the left panel of Figure 14. The correlation coefficient,

747 slope and offset of linear regression fits performed on each comparison orbit are displayed. The correlation of

748 slant columns from BIRA and IUP-UB is extremely high in most cases. It is > 0.998 for all orbits. The slope

749 of the regression line between BIRA and IUP-UB results is close to 1.0. There is a constant offset of less than

750 1×10^{15} molec.cm^{-2}. The comparison between MPIC results and the two other algorithms gives somehow lower

751 correlations, but still larger than 0.98 from the beginning to the end of the OMI lifetime. Final deviations on

752 OMI HCHO SCD when using common settings were found to be of maximum +-2% (slope) and 2.5×10^{15}

753 molec.cm^{-2}. When relating the remaining differences in retrieved SCDs using common settings to the slant

754 column errors from the DOAS fit ($\sigma_{N,s,rand}$), it can be concluded that the differences between the results are

755 significantly smaller than the uncertainties (from 10 to 20% of $\sigma_{N,s,rand}$). Moreover, remaining offsets in SCDs

756 are further reduced by the background correction procedure.
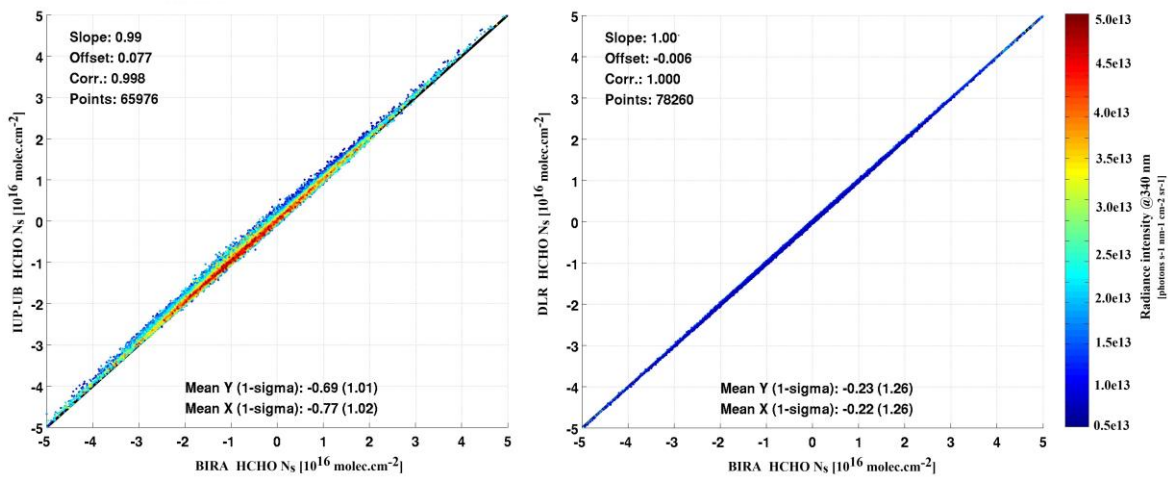
757

758

Figure 13: Correlation (left), slope (middle) and offset (right) from a linear regression performed for the common fit settings (see Table 11) for each orbit of OMI test days. A correlation plot for an example orbit is provided in the left panel of Figure 14.

762 **4.2 Verification of the operational implementation**

763 A similar intercomparison exercise was performed with the operational algorithm UPAS, developed at DLR,

764 but using the exact settings of the prototype algorithm as detailed in Table 2. An example of resulting

765 correlation fit is shown in the right panel of Figure 14 for the same OMI orbit as for the comparison with the

766 IUP-UB results. The level of agreement between the prototype and operational results is found to be almost

767 perfect (correlation coefficient of 1, slope of 1.003 and offset of less than 0.2×10^{15} molec.cm^{-2}), and very

768 satisfactory considering the sensitivity on small implementation changes.

769

Figure 14: Correlation plots of HCHO slant columns retrieved with the BIRA prototype algorithm and (left) the IUP-UB verification algorithm, (right) the operational processor, for OMI orbit number 2339 on 02/02/2005, including all pixels with SZA<80°.

5. Validation

Independent validation activities are proposed and planned by the S5P Validation Team (Fehr, 2016) and within the ESA S5P Mission Performance Center (MPC). The backbone of the formaldehyde validation is the MAX-DOAS and FTIR networks operated as part of the Network for the Detection of Atmospheric Composition Change (NDACC, www.ndsc.ncep.noaa.gov/) complemented by PANDONIA (pandonia.net/) and national activities. In addition, model datasets will be used for validation as well as independent satellite retrievals. Finally, airborne campaigns are planned to support the formaldehyde and other trace gases validation.

5.1 Requirements for validation

To validate the TROPOMI formaldehyde data products, comparisons with independent sources of HCHO measurements are required. This includes comparisons with ground-based measurements, aircraft observations and satellite data sets from independent sensors and algorithms. Moreover, not only information on the total (troposphere) HCHO column is needed but also information on its vertical distribution, especially in the lowest three kilometres where the bulk of formaldehyde generally resides. In this altitude range, the a-priori vertical profile shapes have the largest systematic impact on the satellite column errors. HCHO and aerosol profile measurements are therefore needed.

The diversity of the NMVOC species, lifetimes and sources (biogenic, biomass burning or anthropogenic) calls for validation data in a large range of locations worldwide (tropical, temperate and boreal forests, urban and sub-urban areas). Continuous measurements are needed to obtain good statistics (both for ground-based measurements and for satellite columns) and to capture the seasonal variations. Validation and assessment of consistency with historical satellite datasets require additional information on the HCHO diurnal variation, which depends on the precursor emissions and on the local chemical regime.

796 The main emphasis is on quality assessment of retrieved HCHO column amounts on a global scale and over

797 long time periods. The validation exercise will establish whether HCHO data quality meets the requirements

798 of geophysical research applications like long term trend monitoring on the global scale, NMVOC source

799 inversion, and research on the budget of tropospheric ozone. In addition, the validation will investigate the

800 consistency between TROPOMI HCHO data and HCHO data records from other satellites.

801 **5.2 Reference measurement techniques**

802 Table 12 summarizes the type of data and measurements that can be used for the validation of the TROPOMI

803 HCHO columns. The advantages and limitations of each technique are discussed. It should be noted that, unlike

804 tropospheric O_3 or NO_2, the stratospheric contribution to the total HCHO column can be largely neglected

805 which simplifies the interpretation of both satellite and ground-based measurements.

806 **Table 12: Data/Measurement types used for the validation of satellite HCHO columns. The**

807 **information content of each type of measurement is qualitatively represented by the number of crosses.**

Type of measurement	Sensitivity in the boundary layer	Vertical profile information	Diurnal variation	Seasonal Variation	Total column	Earth coverage
MAX-DOAS	xxx	xx (3)	xxx	xxx	xx	xx
FTIR	x	-	xxx	xx	xxx	x
Direct Sun	xxx	-	xxx	xxx	xxx	x
In situ (1)	xx	-	xxx	xxx	-	xx
Aircraft (2)	xx	xxx	x	-	xx (4)	x
Satellite instruments	x	-	x	xxx	xx	xxx (5)

808

809 (1) Surface measurements that could be combined with regional modelling.

810 (2) Including ultra-light and unmanned airborne vehicles.

811 (3) Up to 2-3 km.

812 (4) Profiles generally need to be extrapolated.

813 (5) Different daily coverage and spatial resolutions.

814 The Multi-axis DOAS (MAX-DOAS) measurement technique has been developed to retrieve stratospheric and

815 tropospheric trace gas total columns and profiles. The most recent generation of MAX-DOAS instruments

816 allows for measurement of aerosols and a number of tropospheric pollutants, such as NO_2, HCHO, SO_2, O_4

817 and CHOCHO (e.g. Irie et al., 2011). With the development of operational networks such as Pandonia

818 (http://pandonia.net/), it is anticipated that many more MAX-DOAS instruments will become available in the

819 near future to extend validation activities in other areas where HCHO emissions are significant. The locations

820 where HCHO measurements are required are reviewed in the next section. Previous comparisons between

821 GOME-2 and OMI HCHO monthly averaged columns with MAX-DOAS measurements recorded by BIRA-

822 IASB in the Beijing city centre and in the sub-urban site of Xianghe showed that the systematic differences

823 between the satellite and ground-based HCHO columns (about 20 to 40%) are almost completely explained

824 when taking into account the vertical averaging kernels of the satellite observations (De Smedt et al., 2015,
825 Wang et al., 2017), showing the importance of validating the a priori profiles as well.

826 HCHO columns can also be retrieved from the ground using FTIR spectrometers. In contrast to MAXDOAS
827 systems which essentially probe the first two kilometres of the atmosphere, FTIR instruments display a strong
828 sensitivity higher up in the free troposphere and are thus complementary to MAXDOAS (Vigouroux et al.,
829 2009). The deployment of FTIR instruments of relevance for HCHO is mostly taking place within the NDACC
830 network. Within the project NIDFORVal (S5P Nitrogen Dioxide and Formaldehyde Validation using NDACC
831 and complementary FTIR and UVVis networks), the number of FTIR stations providing HCHO time-series
832 has been raised from only 4 (Vigouroux et. al, 2009; Jones et al., 2009; Viatte et al., 2014; Franco et al., 2015)
833 to 21. These stations are covering a wide range of HCHO concentrations, from clean Arctic or oceanic sites to
834 sub-urban and urban polluted sites, as well as sites with large biogenic emissions such as Porto Velho (Brazil)
835 or Wollongong (Australia).

836 Although ground-based remote-sensing DOAS and FTIR instruments are naturally best suited for the validation
837 of column measurements from space, in-situ instruments can also bring useful information. This type of
838 instrument can only validate surface HCHO concentrations, and therefore additional information on the vertical
839 profile (e.g. from regional modelling) is required to make the link with the satellite retrieved column. However,
840 in-situ instruments (where available) have the advantage to be continuously operated for pollution monitoring
841 in populated areas, allowing for extended and long term comparisons with satellite data (see e.g. Dufour et al.,
842 2009). Although more expensive and with a limited time and space coverage, aircraft campaigns provide
843 unique information on the HCHO vertical distributions (Zhu et al., 2017).

844 **5.3 Deployment of validation sites**

845 Sites operating correlative measurements should preferably be deployed at locations where significant
846 NMVOC sources exist. This includes:

847 • Tropical forests (Amazonian forest, Africa, Indonesia): The largest HCHO columns worldwide are
848 observed over these remote areas that are difficult to access. Biogenic and biomass burning emissions are
849 mixed. A complete year is needed to discriminate the various effects on the HCHO retrieval. Clouds tend
850 to have more systematic effects in tropical regions. Aircraft measurements are needed over biomass
851 burning areas.

852 • Temperate forests (South-Eastern US, China, Eastern Europe): In summer time, HCHO columns are
853 dominated by biogenic emissions. Those locations are useful to validate particular a-priori assumptions
854 such as model isoprene chemistry and OH oxidation scheme. Measurements are mostly needed from April
855 to September.

856 • Urban and sub-urban areas (Asian cities, California, European cities): Anthropogenic NMVOCs are more
857 diverse, and have a weaker contribution to the total HCHO column than biogenic NMVOCs. This type of
858 signal is therefore more difficult to validate. Continuous observations at mid-latitudes over a full year are
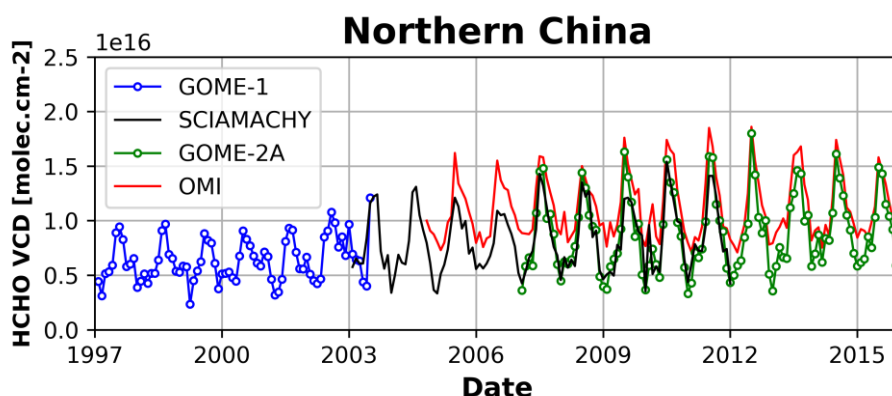859 needed, to improve statistics.

860 For adequate validation, the long-term monitoring should be complemented by dedicated campaigns. Ideally
861 such campaigns should be organised in appropriate locations such as e.g. South-Eastern US, Alabama where
862 biogenic NMVOCs and biogenic aerosols are emitted in large quantities during summer time, and should
863 include both aircraft and ground-based components.

864 **5.4 Satellite-satellite intercomparisons**

865 Satellite-satellite intercomparisons of HCHO columns are generally more straightforward than validation using
866 ground-based correlative measurements. Such comparisons are evaluated in a meaningful statistical sense
867 focusing on global patterns and regional averages, seasonality, scatter of values and consistency between
868 results and reported uncertainties. When intercomparing satellite measurements, special care has to be drawn
869 to:

870 • differences in spatial resolutions, resulting in possible offsets between satellite observations (van
871   der A et al., 2008; De Smedt et al., 2010; Hilboll et al., 2013),
872 • differences in overpass times, that holds valuable geophysical information about diurnal cycles
873   in emissions and chemistry (De Smedt et al., 2015; Stavrakou et al., 2015)
874 • differences in a priori assumptions.
875 • differences in the cloud algorithms and cloud correction schemes.

876 Assessing the consistency between successive satellite sensors is essential to allow for scientific studies making
877 use of the combination of several sensors. For example trends in NVMOC emissions have been successfully
878 derived from GOME(-2), SCIAMACHY, and OMI measurements (Figure 15). It is anticipated that TROPOMI,
879 the next GOME-2 instruments, OMPS, GEMS, TEMPO and the future Sentinel-4 and -5, will allow to extend
880 these time series.

881

882 **Figure 15: HCHO columns over Northern China as observed with GOME (in blue), SCIAMACHY (in**
883 **black), GOME-2 (in green), and OMI (in red) (De Smedt et al., 2008; 2010; 2015).**

6. Conclusions

The retrieval algorithm for the TROPOMI formaldehyde product generation is based on the heritage from algorithms successfully developed for the GOME, SCIAMACHY, GOME-2 and OMI sensors. A double-interval fitting approach is implemented, following an algorithm baseline demonstrated on the GOME-2 and OMI sensors. The HCHO retrieval algorithm also includes a post-processing across-track reference sector correction to minimize OMI-type striping effects, if any. Additional features for future processor updates include the use of a larger fitting interval (if the quality of the recorded spectra allows it), daily earthshine radiance as reference selected in the remote Pacific, spectral outlier screening during the fitting procedure (spike removal algorithm), and a more accurate background correction scheme (as developed for the QA4ECV product).

A detailed uncertainty budget is provided for every satellite observation. The precision of the HCHO tropospheric column is expected to come close to the COPERNICUS product requirements in regions of high emissions and, at mid-latitude, for summer (high sun) conditions. The trueness of the vertical columns is also expected to be improved, owing to the use of daily forecasts for the estimation of HCHO vertical profile shapes, that will be provided by a new version of the TM5-MP model, running at the spatial resolution of 1x1 degree in latitude and longitude.

The validation of satellite retrievals in the lower troposphere is known to be challenging. Ground-based measurements, where available, often sample the atmosphere at different spatial and temporal scales than the satellite measurements, which leads to ambiguous comparisons. Additional correlative measurements are needed over a variety of regions, in particular in the Tropics and at the sub-urban level in mid-latitudes. These aspects are covered by a number of projects developed in the framework of the TROPOMI validation plan (Fehr, 2016).

7. References

Abbot, D. S., Palmer, P. I., Martin, R. V., Chance, K. V., Jacob, D. J. and Guenther, A.: Seasonal and interannual variability of North American isoprene emissions as determined by formaldehyde column measurements from space, Geophys. Res. Lett., 30(17), 1886, 2003.

Anderson, D. C., Nicely, J. M., Wolfe, G. M., Hanisco, T. F., Salawitch, R. J., Canty, T. P., Dickerson, R. R., Apel, E. C., Baidar, S., Bannan, T. J., Blake, N. J., Chen, D., Dix, B., Fernandez, R. P., Hall, S. R., Hornbrook, R. S., Gregory Huey, L., Josse, B., Jöckel, P., Kinnison, D. E., Koenig, T. K., Le Breton, M., Marécal, V., Morgenstern, O., Oman, L. D., Pan, L. L., Percival, C., Plummer, D., Revell, L. E., Rozanov, E., Saiz-Lopez, A., Stenke, A., Sudo, K., Tilmes, S., Ullmann, K., Volkamer, R., Weinheimer, A. J. and Zeng, G.: Formaldehyde in the Tropical Western Pacific: Chemical Sources and Sinks, Convective Transport, and Representation in CAM-Chem and the CCMI Models, J. Geophys. Res. Atmos., 122(20), 11,201-11,226, doi:10.1002/2016JD026121, 2017.

Barkley, M. P., Palmer, P. I., Ganzeveld, L., Arneth, A., Hagberg, D., Karl, T., Guenther, A., Paulot, F., Wennberg, P. O., Mao, J., Kurosu, T. P., et al.: Can a state of the art chemistry transport model simulate Amazonian tropospheric chemistry?, J. Geophys. Res., 116(D16), D16302, doi:10.1029/2011JD015893, 2011.

Barkley, M. P., Kurosu, T. P., Chance, K., Smedt, I. De, Van Roozendael, M., Arneth, A., Hagberg, D., Guenther, A. and De Smedt, I.: Assessing sources of uncertainty in formaldehyde air mass factors over tropical South America: Implications for top-down isoprene emission estimates, J. Geophys. Res., 117(D13), D13304, doi:10.1029/2011JD016827, 2012.

Barkley, M. P., De Smedt, I., Van Roozendael, M., Kurosu, T. P., Chance, K. V, Arneth, A., Hagberg, D., Guenther, A. B., Paulot, F., Marais, E. A., others, et al.: Top-down isoprene emissions over tropical South America inferred from SCIAMACHY and OMI formaldehyde columns, J. Geophys. Res. Atmos., 118(12), n/a–n/a, doi:10.1002/jgrd.50552, 2013.

Boersma, K. F., Eskes, H. J. and Brinksma, E. J.: Error analysis for tropospheric NO2 retrieval from space, J. Geophys. Res., 109(D4), doi:10.1029/2003JD003962, 2004.

Boersma, K.F., Lorente, A., Muller, J. and the QA4ECV consortium: Recommendations (scientific) on best practices for retrievals for Land and Atmosphere ECVs, QA4ECV D4.2, v0.8, http://www.qa4ecv.eu/sites/default/files/D4.2.pdf, 2015.

Boersma, K. F., Vinken, G. C. M., and Eskes, H. J.: Representativeness errors in comparing chemistry transport and chemistry climate models with satellite UV–Vis tropospheric column retrievals, Geosci. Model Dev., 9, 875-898, https://doi.org/10.5194/gmd-9-875-2016, 2016.

Bovensmann, H., Peuch, V.-H., van Weele, M., Erbertseder, T., and Veihelmann, B.: Report Of The Review Of User Requirements For Sentinels-4/-5, ESA, EO-SMA-/1507/JL, issue: 2.1, 2011.

945 Brion, J., et al.: Absorption spectra measurements for the ozone molecule in the 350-830 nm region, J. Atmos.
946 Chem., 30, 291-299, 1998.

947 Castellanos, P., Boersma, K. F., Torres, O., and de Haan, J. F.: OMI tropospheric NO2 air mass factors over
948 South America: effects of biomass burning aerosols, Atmos. Meas. Tech., 8, 3831-3849, doi:10.5194/amt-8-
949 3831-2015, 2015.

950 Chance, K. and R. J. Spurr: Ring effect studies: Rayleigh scattering including molecular parameters for
951 rotational Raman scattering, and the Fraunhofer spectrum, Applied Optics, 36, 5224-5230, 1997.

952 Chance, K. V., Palmer, P. I., Martin, R. V., Spurr, R. J. D., Kurosu, T. P. and Jacob, D. J.: Satellite observations
953 of formaldehyde over North America from GOME, Geophysical Research Letters, 27(21), 3461-3464,
954 doi:10.1029/2000GL011857, 2000.

955 Chance, K. and Kurucz, R. L.: An improved high-resolution solar reference spectrum for earth's atmosphere
956 measurements in the ultraviolet, visible, and near infrared, J. Quant. Spectrosc. Radiat. Transf., 111(9), 1289-
957 1295, 2010.

958 Chimot, J., Vlemmix, T., Veefkind, J. P., de Haan, J. F. and Levelt, P. F.: Impact of aerosols on the OMI
959 tropospheric NO2 retrievals over industrialized regions: how accurate is the aerosol correction of cloud-free
960 scenes via a simple cloud model?, Atmos. Meas. Tech. Discuss., 8(8), 8385–8437, doi:10.5194/amtd-8-8385-
961 2015, 2015.

962 Clémer, K., Van Roozendael, M., Fayt, C., Hendrick, F., Hermans, C., Pinardi, G., Spurr, R., Wang, P., and
963 De Mazière, M.: Multiple wavelength retrieval of tropospheric aerosol optical properties from MAXDOAS
964 measurements in Beijing, Atmos. Meas. Tech., 3, 863-878, 2010.

965 Curci, G., Palmer, P. I., Kurosu, T. P., Chance, K. and Visconti, G.: Estimating European volatile organic
966 compound emissions using satellite observations of formaldehyde from the Ozone Monitoring Instrument,
967 Atmos. Chem. Phys., 10(23), 11501-11517, 2010.

968 Danckaert, T., Fayt, C., Van Roozendael, M., De Smedt, I., Letocart, V., Merlaud, A., Pinardi, G: Qdoas
969 Software User Manual, Version 2.1, http://uv-
970 vis.aeronomie.be/software/QDOAS/QDOAS_manual_2.1_201212.pdf, 2012.

971 Danielson, J.J., and Gesch, D.B.: Global multi-resolution terrain elevation data 2010 (GMTED2010): U.S.
972 Geological Survey Open-File Report 2011–1073, 26 p, 2011.

973 Daumont, M., Brion, J., Charbonnier, J., and Malicet, J.: Ozone UV spectroscopy, I: Absorption cross-sections
974 at room temperature, J. Atmos. Chem., 15, 145–155, 1992.

975 De Smedt, I., Müller, J.-F., Stavrakou, T., van der A, R., Eskes, H. and Van Roozendael, M.: Twelve years of
976 global observations of formaldehyde in the troposphere using GOME and SCIAMACHY sensors, Atmos.
977 Chem. Phys., 8(16), 4947-4963, 2008.

978 De Smedt, I., Stavrakou, T., Müller, J. F., van Der A, R. J. and Van Roozendael, M.: Trend detection in satellite
979 observations of formaldehyde tropospheric columns, Geophys. Res. Lett., 37(18), L18808,
980 doi:10.1029/2010GL044245, 2010.

981 De Smedt, I.: Long-Term Global Observations of Tropospheric Formaldehyde Retrieved from Spaceborne
982 Nadir UV Sensors, Ph.D. thesis, Universite Libre De Bruxelles, Laboratoire do Chimie Quantique et
983 Photophysique, Facultéé de Sciences Appliquées, 2011.

984 De Smedt, I., Van Roozendael, M., Stavrakou, T., Müller, J.-F., Lerot, C., Theys, N., Valks, P., Hao, N., and
985 van der A, R.: Improved retrieval of global tropospheric formaldehyde columns from GOME-2/MetOp-A
986 addressing noise reduction and instrumental degradation issues, Atmos. Meas. Tech. Discuss., 5, 5571-5616,
987 doi:10.5194/amtd-5-5571-2012, Special Issue: GOME-2: calibration, algorithms, data products and validation,
988 2012.

989 De Smedt, I., Stavrakou, T., Hendrick, F., Danckaert, T., Vlemmix, T., Pinardi, G., Theys, N., Lerot, C., Gielen,
990 C., Vigouroux, C., Hermans, C., et al.: Diurnal, seasonal and long-term variations of global formaldehyde
991 columns inferred from combined OMI and GOME-2 observations, Atmos. Chem. Phys. Discuss., 15(8),
992 12241–12300, doi:10.5194/acpd-15-12241-2015, 2015.

993 De Smedt, I., Theys, N., van Gent, J., Danckaert, T., Yu, H. and Van Roozendael, M.: S5P/TROPOMI HCHO
994 ATBD, S5P-BIRA-L2-400F-ATBD, v1.0.0, 2016-02-19, Level-2 Algorithm Developments for Sentinel-5
995 Precursor.,   http://www.tropomi.eu/sites/default/files/files/S5P-BIRA-L2-ATBD-
996 HCHO_400F_TROPOMI_v1p0p0-20160205.pdf , 2016.

997 Dirksen, R., Dobber, M., Voors, R., and Levelt, P.: Prelaunch characterization of the Ozone Monitoring
998 Instrument transfer function in the spectral domain, Appl. Opt., 45(17), 3972-3981, 2006.

999 Dufour, G., F. Wittrock, M. Camredon, M. Beekmann, A. Richter, B. Aumont, and J. P. Burrows,
1000 SCIAMACHY formaldehyde observations: constraint for isoprene emission estimates over Europe?, Atmos.
1001 Chem. Phys., 9(5), 1647-1664, 2009.

1002 Eskes, H. J. and K. F. Boersma, Averaging kernels for DOAS total-column satellite retrievals, Atmos. Chem.
1003 Phys., 3, 1285-1291, 2003.

1004 Fayt, C. and M. Van Roozendael: Windoas 2.1, Software User Manual, BIRA-IASB, 2001.

1005 Fehr, T.: Sentinel-5 Precursor Scientific Validation Implementation Plan, EOP-SM/2993/TF-tf, 1.0,
1006 http://doi.org/10.5281/zenodo.165739, 2016.

1007   Fleischmann, O. C., et al.: New ultraviolet absorption cross-sections of BrO at atmospheric temperatures
1008   measured by time-windowing Fourier transform spectroscopy, J. Photochem. Photobiol. A, 168, 117–132,
1009   2004.

1010   Fortems-Cheiney, A., Chevallier, F., Pison, I., Bousquet, P., Saunois, M., Szopa, S., Cressot, C., Kurosu, T. P.,
1011   Chance, K. and Fried, A.: The formaldehyde budget as seen by a global-scale multi-constraint and multi-
1012   species inversion system, Atmos. Chem. Phys. Discuss., 12(3), 6909-6955, doi:10.5194/acpd-12-6909-2012,
1013   2012.

1014   Franco, B., Hendrick, F., Van Roozendael, M., Müller, J.-F., Stavrakou, T., Marais, E. A., Bovy, B., Bader,
1015   W., Fayt, C., Hermans, C., Lejeune, B., Pinardi, G., Servais, C., and Mahieu, E.: Retrievals of formaldehyde
1016   from ground-based FTIR and MAX-DOAS observations at the Jungfraujoch station and comparisons with
1017   GEOS-Chem   and   IMAGES   model   simulations,   Atmos.   Meas.   Tech.,   8,   1733-1756,
1018   https://doi.org/10.5194/amt-8-1733-2015, 2015.

1019   Fu, T.-M., Jacob, D. J., Palmer, P. I., Chance, K. V., Wang, Y. X., Barletta, B., Blake, D. R., Stanton, J. C. and
1020   Pilling, M. J.: Space-based formaldehyde measurements as constraints on volatile organic compound emissions
1021   in east and south Asia and implications for ozone, J. Geophys. Res., 112(D6), D06312, 2007.

1022   González Abad, G., Liu, X., Chance, K., Wang, H., Kurosu, T. P. and Suleiman, R.: Updated Smithsonian
1023   Astrophysical Observatory Ozone Monitoring Instrument (SAO OMI) formaldehyde retrieval, Atmos. Meas.
1024   Tech., 8(1), 19–32, doi:10.5194/amt-8-19-2015, 2015.

1025   González Abad, G., Vasilkov, A., Seftor, C., Liu, X., and Chance, K.: Smithsonian Astrophysical Observatory
1026   Ozone Mapping and Profiler Suite (SAO OMPS) formaldehyde retrieval, Atmos. Meas. Tech., 9, 2797-2812,
1027   https://doi.org/10.5194/amt-9-2797-2016, 2016.

1028   Gonzi, S., Palmer, P. I., Barkley, M. P., De Smedt, I. and Van Roozendael, M.: Biomass burning emission
1029   estimates inferred from satellite column measurements of HCHO: Sensitivity to co-emitted aerosol and
1030   injection height, Geophys. Res. Lett., 38(14), L14807, doi:10.1029/2011GL047890, 2011.

1031   Gottwald, M., Bovensmann, H. et al.: SCIAMACHY, Monitoring the Changing Earth's Atmosphere, DLR,
1032   Institut für Methodik der Fernerkundung (IMF), 2006.

1033   Grainger, J. F. and J. Ring: Anomalous Fraunhofer line profiles, Nature, 193, 762, 1962.

1034   Greenblatt, G. D., Orlando, J. J., Burkholder, J. B., and Ravishankara, A. R.: Absorption measurements of
1035   oxygen between 330 and 1140 nm, J. Geophys. Res., 95(D11), 18 577–18 582, doi:10.1029/90JD01375, 1990.

1036   Hartmann, D. L., Klein Tank, A.M. G., Rusticucci, M., Alexan- der, L. V., Brönnimann, S., Charabi, Y.,
1037   Dentener, F. J., Dlugo- kencky, E. J., Easterling, D. R., Kaplan, A., Soden, B. J., Thorne, P.W.,Wild, M., and
1038   Zhai, P. M.: Observations: Atmosphere and Surface, in: Climate Change 2013: The Physical Science Basis.

Contribution of Working Group I to the Fifth Assessment Report of the Intergovernmental Panel on Climate Change, edited by: Stocker, T. F., Qin, D., Plattner, G.-K., Tignor, M., Allen, S. K., Boschung, J., Nauels, A., Xia, Y., Bex, V., and Midgley P. M., Cambridge University Press, Cambridge, United Kingdom and New York, NY, USA, 2013.

Hassinen, S., Balis, D., Bauer, H., Begoin, M., Delcloo, A., Eleftheratos, K., Gimeno Garcia, S., Granville, J., Grossi, M., Hao, N., Hedelt, P., Hendrick, F., Hess, M., Heue, K.-P., Hovila, J., Jønch-Sørensen, H., Kalakoski, N., Kauppi, A., Kiemle, S., Kins, L., Koukouli, M. E., Kujanpää, J., Lambert, J.-C., Lang, R., Lerot, C., Loyola, D., Pedergnana, M., Pinardi, G., Romahn, F., Van Roozendael, M., Lutz, R., De Smedt, I., Stammes, P., Steinbrecht, W., Tamminen, J., Theys, N., Tilstra, L. G., Tuinder, O. N. E., Valks, P., Zerefos, C., Zimmer, W. and Zyrichidou, I.: Overview of the O3M SAF GOME-2 operational atmospheric composition and UV radiation data products and data availability, Atmos. Meas. Tech., 9(2), 383–407, doi:10.5194/amt-9-383-2016, 2016.

Heckel, A., Kim, S.-W., Frost, G. J., Richter, A., Trainer, M. and Burrows, J. P.: Influence of low spatial resolution a priori data on tropospheric NO2 satellite retrievals, Atmos. Meas. Tech., 4(9), 1805–1820, doi:10.5194/amt-4-1805-2011, 2011.

Hewson, W., Bösch, H., Barkley, M. P. and De Smedt, I.: Characterisation of GOME-2 formaldehyde retrieval sensitivity, Atmospheric Measurement Techniques, 6(2), 371–386, doi:10.5194/amt-6-371-2013, 2013.

Hilboll, A., Richter, A. and Burrows, J. P.: Long-term changes of tropospheric NO2 over megacities derived from multiple satellite instruments, Atmospheric Chemistry and Physics, 13(8), 4145–4169, doi:10.5194/acp-13-4145-2013, 2013.

Huijnen, V., Williams, J., van Weele, M., van Noije, T., Krol, M., Dentener, F., Segers, A., Houweling, S., Peters, W., de Laat, J., Boersma, F., Bergamaschi, P., van Velthoven, P., Le Sager, P., Eskes, H., Alkemade, F., Scheele, R., Nédélec, P., and Pätz, H.-W., The global chemistry transport model tm5: description and evaluation of the tropospheric chemistry version 3.0., Geoscientific Model Development, 3(2):445-473, 2010.

Jones, N. B., Riedel, K., Allan, W., Wood, S., Palmer, P. I., Chance, K., and Notholt, J.: Long-term tropospheric formaldehyde concentrations deduced from ground-based fourier transform solar infrared measurements, Atmos. Chem. Phys., 9, 7131-7142, https://doi.org/10.5194/acp-9-7131-2009, 2009.

Kaiser, J., Jacob, D. J., Zhu, L., Travis, K. R., Fisher, J. A., González Abad, G., Zhang, L., Zhang, X., Fried, A., Crounse, J. D., St. Clair, J. M., and Wisthaler, A.: High-resolution inversion of OMI formaldehyde columns to quantify isoprene emission on ecosystem-relevant scales: application to the Southeast US, Atmos. Chem. Phys. Discuss., https://doi.org/10.5194/acp-2017-1137, in review, 2017

Kleipool, Q. L., Dobber, M. R., de Haan, J. F. and Levelt, P. F.: Earth surface reflectance climatology from 3 years of OMI data, J. Geophys. Res., 113(D18), D18308, doi:10.1029/2008JD010290, 2008.

1072 Koelemeijer, R. B. A., Stammes, P., Hovenier, J. W. and de Haan, J. F.: A fast method for retrieval of cloud
1073 parameters using oxygen A band measurements from the Global Ozone Monitoring Experiment, J. Geophys.
1074 Res., 106(D4), 3475-3490, doi:10.1029/2000JD900657, 2001.

1075 Khokhar, M. F.: Spatio-Temporal Analyses of Formaldehyde over Pakistan by Using SCIAMACHY and
1076 GOME-2 Observations, Aerosol Air Qual. Res., 1–14, doi:10.4209/aaqr.2014.12.0339, 2015.

1077 Krol, M., Houweling, S., Bregman, B., van den Broek, M., Segers, A., van Velthoven, P., Peters, W., Dentener,
1078 F., and Bergamaschi, P.: The two-way nested global chemistry-transport zoom model TM5: algorithm and
1079 applications., Atmos. Chem. Phys., 5(2):417-432, 2005.

1080 Kurosu, T. P., OMHCHO README FILE,
1081 http://www.cfa.harvard.edu/tkurosu/SatelliteInstruments/OMI/PGEReleases/READMEs/OMHCHO_READ
1082 ME.pdf, last access: 14/08/2012, 2008.

1083 Langen, J., Meijer, Y., Brinksma, E., Veihelmann, B., and Ingmann, P.: GMES Sentinels 4 and 5 Mission
1084 Requirements Document (MRD), ESA, EO-SMA-/1507/JL, issue: 3, 2011.

1085 Langen, J., Meijer, Y., Brinksma, E., Veihelmann, B., and Ingmann, P.: Copernicus Sentinels 4 and 5 Mission
1086 Requirements Traceability Document (MRTD), ESA, EO-SMA-/1507/JL, issue: 2, 2017.

1087 Leitao, J., Richter, A., Vrekoussis, M., Kokhanovsky, A., Zhang, Q.J., Beekmann, M., and Burrows, J. P.: On
1088 the improvement of NO2 satellite retrievals – aerosol impact on the airmass factors, Atmos. Meas. Tech., 3,
1089 475–493, doi:10.5194/amt-3-475-2010,2010.

1090 Leue, C.: Detektion der troposphärischen NO2 Daten anhand von GOME. Ph.D. thesis, Univ. Heidelberg,
1091 Heidelberg, Germany, 1999.

1092 Li, C., Joiner, J., Krotkov, N. A. and Dunlap, L.: A New Method for Global Retrievals of HCHO Total Columns
1093 from the Suomi National Polar-orbiting Partnership Ozone Monitoring and Profiler Suite, Geophys. Res. Lett.,
1094 doi:10.1002/2015GL063204, 2015.

1095 Lin, J. T., Martin, R. V., Boersma, K. F., Sneep, M., Stammes, P., Spurr, R., Wang, P., Van Roozendael, M.,
1096 Clemer, K. and Irie, H.: Retrieving tropospheric nitrogen dioxide from the Ozone Monitoring Instrument:
1097 Effects of aerosols, surface reflectance anisotropy, and vertical profile of nitrogen dioxide, Atmos. Chem.
1098 Phys., 14(3), 1441–1461, doi:10.5194/acp-14-1441-2014, 2014.

1099 Lorente, A., Boersma, K. F., Yu, H., Dörner, S., Hilboll, A., Richter, A., Liu, M., Lamsal, L. N., Barkley, M.,
1100 De Smedt, I., Van Roozendael, M., Wang, Y., Wagner, T., Beirle, S., Lin, J. T., Kroktov, N., Stammes, P.,
1101 Wang, P., Eskes, H. J., and Krol, M.: Structural uncertainty in air mass factor calculation for NO2 and HCHO
1102 satellite retrievals, Atmos. Meas. Tech. Discuss., doi:10.5194/amt-2016-306, in review, 2016.

1103   Loyola, D. G., Gimeno García, S., Lutz, R., Romahn, F., Spurr, R. J. D., Pedergnana, M., Doicu, A., and

1104   Schüssler, O.: The operational cloud retrieval algorithms from TROPOMI on board Sentinel-5 Precursor,

1105   Atmos. Meas. Tech. Discuss., https://doi.org/10.5194/amt-2017-128, in review, 2017.

1106   Mahajan, A. S., De Smedt, I., Biswas, M. S., Ghude, S., Fadnavis, S., Roy, C. and van Roozendael, M.: Inter-

1107   annual variations in satellite observations of nitrogen dioxide and formaldehyde over India, Atmos. Environ.,

1108   116, 194–201, doi:10.1016/j.atmosenv.2015.06.004, 2015.

1109   Malicet, C., Daumont, D., Charbonnier, J., Parisse, C., Chakir, A., and Brion, J.: Ozone UV spectroscopy, II:

1110   Absorption cross-sections and temperature dependence, J. Atmos. Chem., 21, 263–273, 1995.

1111   Marais, E. A., Jacob, D. J., Kurosu, T. P., Chance, K., Murphy, J. G., Reeves, C., Mills, G., Casadio, S., Millet,

1112   D. B., Barkley, M. P., Paulot, F., et al.: Isoprene emissions in Africa inferred from OMI observations of

1113   formaldehyde columns, Atmos. Chem. Phys. Discuss., 12(3), 7475-7520, doi:10.5194/acpd-12-7475-2012,

1114   2012.

1115   Marbach, T., Beirle, S., Platt, U., Hoor, P., Wittrock, F., Richter, A., Vrekoussis, M., Grzegorski, M., Burrows,

1116   J. P. and Wagner, T.: Satellite measurements of formaldehyde linked to shipping emissions, Atmos. Chem.

1117   Phys., 9(21), 2009.

1118   Martin, R. V, Chance, K. V, Jacob, D. J., Kurosu, T. P., Spurr, R. J. D., Bucsela, E. J., Gleason, J., Palmer, P.

1119   I., Bey, I., Fiore, A. M., Li, Q., et al.: An improved retrieval of tropospheric nitrogen dioxide from GOME, J.

1120   Geophys. Res., 107(D20), doi:10.1029/2001JD001027, 2002.

1121   Meller, R., and Moortgat, G. K.: Temperature dependence of the absorption cross section of HCHO between

1122   223 and 323K in the wavelength range 225–375 nm, J. Geophys. Res., 105(D6), 7089–7102,

1123   doi:10.1029/1999JD901074, 2000.

1124   Millet, D. B., Jacob, D. J., Boersma, K. F., Fu, T.-M., Kurosu, T. P., Chance, K. V., Heald, C. L. and Guenther,

1125   A.: Spatial distribution of isoprene emissions from North America derived from formaldehyde column

1126   measurements by the OMI satellite sensor, Journal of Geophysical Research, 113(D2), 1-18,

1127   doi:10.1029/2007JD008950, 2008.

1128   Palmer, P. I., Jacob, D. J., Chance, K. V., Martin, R. V., D, R. J., Kurosu, T. P., Bey, I., Yantosca, R. and Fiore,

1129   A.: Air mass factor formulation for spectroscopic measurements from satellites: Application to formaldehyde

1130   retrievals from the Global Ozone Monitoring Experiment, Journal of Geophysical Research, 106(D13), 14539-

1131   14550, doi:10.1029/2000JD900772, 2001.

1132   Palmer, P. I., Abbot, D. S., Fu, T.-M., Jacob, D. J., Chance, K. V., Kurosu, T. P., Guenther, A., Wiedinmyer,

1133   C., Stanton, J. C., Pilling, M. J., Pressley, S. N., et al.: Quantifying the seasonal and interannual variability of

1134   North American isoprene emissions using satellite observations of the formaldehyde column, Journal of

1135   Geophysical Research, 111(D12), 1-14, doi:10.1029/2005JD006689, 2006.

1136 Pedergnana, M., Loyola, D., Apituley, A., Sneep, M., Veefkind, J. P.: Sentinel-5 precursor/TROPOMI Level
1137 2 Product User Manual Formaldehyde HCHO, S5P-L2-DLR-PUM-400F, 0.11.4,
1138 http://www.tropomi.eu/sites/default/files/files/S5P-L2-DLR-PUM-400F-
1139 Product_User_Manual_for_the_Sentinel_5_precursor_Formaldehyde_HCHO-00.11.04-
1140 20170601_signed.pdf, 2017.

1141 Pinardi, G., Van Roozendael, M., Abuhassan, N., Adams, C., Cede, a., Clémer, K., Fayt, C., Frieß, U., Gil, M.,
1142 Herman, J., Hermans, C., et al.: MAX-DOAS formaldehyde slant column measurements during CINDI:
1143 intercomparison and analysis improvement, Atmospheric Measurement Techniques, 6(1), 167–185,
1144 doi:10.5194/amt-6-167-2013, 2013.

1145 Platt, U.: Differential optical absorption spectroscopy (DOAS), in Air Monitoring by Spectroscopic
1146 Techniques, M.W. Sigrist ed., Chemical Analysis Series, Wiley, New York, 127, 27-84, 1994.

1147 Platt, U and Stutz, J.: Differential Optical Absorption Spectroscopy: Principles and Applications (Physics of
1148 Earth and Space Environments), Springer-Verlag, Berlin, Heidelberg, ISBN 978-3540211938, 2008.

1149 Puķīte, J., Kühl, S., Deutschmann, T., Platt, U., and Wagner, T.: Extending differential optical absorption
1150 spectroscopy for limb measurements in the UV, Atmos. Meas. Tech., 3, 631-653, 2010.

1151 Richter, A., Begoin, M., Hilboll, A. and Burrows, J. P.: An improved NO2 retrieval for the GOME-2 satellite
1152 instrument, Atmos. Meas. Tech., 4(6), 213-246, doi:10.5194/amt-4-1147-2011, 2011.

1153 Richter, A. and S5-P verification teams: S5P/TROPOMI Science Verification Report, S5P-IUP-L2-ScVR-RP,
1154 v2.1, 2015-12-22, in Level-2 Algorithm Developments for Sentinel-5 Precursor., 2015.

1155 Rodgers, C. D.: Inverse Methods for Atmospheric Sounding, Theory and Practice, World Scientific Publishing,
1156 Singapore-New-Jersey-London-Hong Kong, 2000.

1157 Rodgers, C. D., and B. J. Connor: Intercomparison of remote sounding instruments, J. Geophys. Res., 108,
1158 doi:10.1029/2002JD002299, 2003.

1159 Seinfeld, J. H. and S. N. Pandis, Atmospheric Chemistry and Physics: From air pollution to climate change,
1160 second edition, John Wiley and Sons, New-York, 2006.

1161 Serdyuchenko, A., Gorshelev, V., Weber, M., Chehade, W., and Burrows, J. P.: High spectral resolution ozone
1162 absorption cross-sections – Part 2: Temperature dependence, Atmos. Meas. Tech., 7, 625-636,
1163 doi:10.5194/amt-7-625-2014, 2014.

1164 Spurr, R. J. D.: LIDORT and VLIDORT: Linearized pseudo-spherical scalar and vector discrete ordinate
1165 radiative transfer models for use in remote sensing retrieval problems, in Light Scattering Reviews, edited by
1166 A. Kokhanovsky, pp. 229–271, Berlin, 2008a.

1167 Spurr, R. J. D., J. de Haan, R. van Oss, and A. Vasilkov, Discrete ordinate radiative transfer in a stratified
1168 medium with first-order rotational Raman scattering, J.Q.S.R.T 109, Iss. 3, 404425, 2008b.

1169 Stavrakou, T., Müller, J. F., De Smedt, I., Van Roozendael, M., van der Werf, G. R., Giglio, L. and Guenther,
1170 A.: Global emissions of non-methane hydrocarbons deduced from SCIAMACHY formaldehyde columns
1171 through 2003–2006, Atmos. Chem. Phys., 9(3), 1037-1060, 2009a.

1172 Stavrakou, T., Smedt, I. D., Roozendael, M. V., Vrekoussis, M., Wittrock, F., Burrows, J., Building, M., Lane,
1173 B., Gifford, C. and Kingdom, U.: The continental source of glyoxal estimated by the synergistic use of
1174 spaceborne measurements and inverse modelling, 2009b.

1175 Stavrakou, T., Müller, J.-F., Bauwens, M., De Smedt, I., Van Roozendael, M., Guenther, a., Wild, M. and Xia,
1176 X.: Isoprene emissions over Asia 1979–2012: impact of climate and land-use changes, Atmos. Chem. Phys.,
1177 14(9), 4587–4605, doi:10.5194/acp-14-4587-2014, 2014.

1178 Stavrakou, T., Müller, J., Bauwens, M., Smedt, I. De and Roozendael, M. Van: How consistent are top-down
1179 hydrocarbon emissions based on formaldehyde observations from GOME-2 and OMI ?, Atmos. Chem. Phys.
1180 Discuss., 12007–12067, doi:10.5194/acpd-15-12007-2015, 2015.

1181 Stein Zweers et al., TROPOMI ATBD of the UV aerosol index, S5P-KNMI-L2-0008-RP, 1.0,
1182 http://www.tropomi.eu/sites/default/files/files/S5P-KNMI-L2-0008-RP-TROPOMI_ATBD_UVAI-v1p0p0-
1183 20160203.pdf, 2016

1184 Tanskanen, A. Lambertian Surface Albedo Climatology at 360 nm from TOMS Data Using Moving Time-
1185 Window Technique. In: Proceedings of the XX Quadrennial Ozone Symposium, 1-8 June 2004, Kos, Greece.

1186 Thalman, R. and Volkamer, R.: Temperature dependent absorption cross-sections of O2-O2 collision pairs
1187 between 340 and 630 nm and at atmospherically relevant pressure., Phys. Chem. Chem. Phys., 15(37), 15371–
1188 81, doi:10.1039/c3cp50968k, 2013.

1189 Theys, N., De Smedt, I., Yu, H., Danckaert, T., van Gent, J., Hörmann, C., Wagner, T., Hedelt, P., Bauer, H.,
1190 Romahn, F., Pedergnana, M., Loyola, D. and Van Roozendael, M.: Sulfur dioxide retrievals from TROPOMI
1191 onboard Sentinel-5 Precursor: algorithm theoretical basis, Atmos. Meas. Tech., 10(January), 119–153,
1192 doi:10.5194/amt-10-119-2017, 2017.

1193 U.S. Standard Atmosphere, U.S. Government Printing Office, Washington, D.C., 1976.

1194 Vandaele A.C., C. Hermans, P.C. Simon, M. Carleer, R. Colin, S. Fally, M.F. Mérienne, A. Jenouvrier, and B.
1195 Coquart, Measurements of the NO2 absorption cross-section from 42000 cm-1 to 10000 cm-1 (238-1000 nm)
1196 at 220 K and 294 K, J.Q.S.R.T., 59, 171-184, 1998.

1197   van der A, R.J., H.J. Eskes, K.F. Boersma, T.P. van Noije, et al., Trends, seasonal variability and dominant

1198   NOx source derived from a ten year record of NO_2 measured from space, J. Geophys. Res., 113, D04302, doi:

1199   10.1029/2007JD009021, 2008.

1200   van Geffen, J.H.G.M., K.F. Boersma, H.J. Eskes, J.D. Maasakkers and J.P. Veefkind, TROPOMI ATBD of

1201   the total and tropospheric NO2 data products, S5P-KNMI-L2-0005-RP, 1.1.0,

1202   http://www.tropomi.eu/sites/default/files/files/S5P-KNMI-L2-0005-RP-

1203   TROPOMI_ATBD_NO2_data_products-v1p1p0-20170816_signed.pdf, 2017.

1204   Van Roozendael, M., V. Soebijanta, C. Fayt, and J.-C. Lambert: Investigation of DOAS Issues Affecting the

1205   Accuracy of the GDP Version 3.0 Total Ozone Product, in ERS-2 GOME GDP 3.0 Implementation and Delta

1206   Validation, ERSE-DTEX-EOAD-TN-02-0006, ESA/ESRIN, Frascati, Italy, Chap.6, pp.97-129, 2002.

1207   Van Roozendael, M., Spurr, R., Loyola, D., Lerot, C., Balis, D., Lambert, J.-C., Zimmer, W., Van Gent, J.,

1208   Van Geffen, J., Koukouli, M., Granville, J., Doicu, A., Fayt, C. & Zehner, C.: Sixteen Years Of GOME/ERS-

1209   2 Total Ozone Data: The New Direct-Fitting Gome Data Processor (Gdp) Version 5 - Algorithm Description,

1210   J.geophys. Res., 117, D03305, Doi: 10.1029/2011jd016471, 2012.

1211   van Weele, M., Levelt, P., Aben, I., Veefkind, P., Dobber, M., Eskes, H., Houweling, S., Landgraf, J.,

1212   Noordhoek, R. : Science Requirements Document for TROPOMI. Volume 1, KNMI & SRON, RS-

1213   TROPOMI-KNMI-017, issue: 2.0, 2008.

1214   Veefkind, J. P., Aben, I., McMullan, K., Förster, H., de Vries, J., Otter, G., Claas, J., Eskes, H. J., de Haan, J.

1215   F., Kleipool, Q., van Weele, M., et al.: TROPOMI on the ESA Sentinel-5 Precursor: A GMES mission for

1216   global observations of the atmospheric composition for climate, air quality and ozone layer applications,

1217   Remote Sensing of Environment, 120(0), 70-83, 2012.

1218   Veefkind, J. P., de Haan, J. F., Sneep, M., and Levelt, P. F.: Improvements to the OMI O2–O2 operational

1219   cloud algorithm and comparisons with ground-based radar–lidar observations, Atmos. Meas. Tech., 9, 6035-

1220   6049, https://doi.org/10.5194/amt-9-6035-2016, 2016.

1221   Viatte, C., Strong, K., Walker, K. A., and Drummond, J. R.: Five years of CO, HCN, C2H6, C2H2, CH3OH,

1222   HCOOH and H2CO total columns measured in the Canadian high Arctic, Atmos. Meas. Tech., 7, 1547-1570,

1223   https://doi.org/10.5194/amt-7-1547-2014, 2014.

1224   Vigouroux, C., F. Hendrick, T. Stavrakou, B. Dils, I. De Smedt, C. Hermans, A. Merlaud, F. Scolas, C. Senten,

1225   G. Vanhaelewyn, S. Fally, M. Carleer, J.-M. Metzger, J.-F. Müller, M. Van Roozendael, and M. De Mazière,

1226   Ground-based FTIR and MAX-DOAS observations of formaldehyde at Réunion Island and comparisons with

1227   satellite and model data, Atmos. Chem. Phys., 9, 9523-9544, doi:10.5194/acp-9-9523-2009.

1228   Vountas, M., Rozanov, V. V. and Burrows, J. P.: Ring effect: impact of rotational Raman scattering on radiative

1229   transfer in earth's atmosphere, J. of Quant. Spec. and Rad. Trans., 60(6), 943-961, 1998.

1230 Vrekoussis, M., Wittrock, F., Richter, A. and Burrows, J. P.: GOME-2 observations of oxygenated VOCs:
1231 what can we learn from the ratio glyoxal to formaldehyde on a global scale?, Atmos. Chem. Phys., 10(21),
1232 10145-10160, 2010.

1233 Williams, J. E., Boersma, K. F., Le Sager, P., and Verstraeten, W. W.: The high-resolution version of TM5-
1234 MP for optimized satellite retrievals: description and validation, Geosci. Model Dev., 10, 721-750,
1235 doi:10.5194/gmd-10-721-2017, 2017.

1236 Wittrock, F., Richter, A., Oetjen, H., Burrows, J. P., Kanakidou, M., Myriokefalitakis, S., Volkamer, R., Beirle,
1237 S., Platt, U. and Wagner, T.: Simultaneous global observations of glyoxal and formaldehyde from space,
1238 Geophysical Research Letters, 33(16), 1-5, doi:10.1029/2006GL026310, 2006.

1239 Zhu, L., Jacob, D. J., Kim, P. S., Fisher, J. A., Yu, K., Travis, K. R., Mickley, L. J., Yantosca, R. M., Sulprizio,
1240 M. P., De Smedt, I., Gonzalez Abad, G., Chance, K., Li, C., Ferrare, R., Fried, A., Hair, J. W., Hanisco, T. F.,
1241 Richter, D., Scarino, A. J., Walega, J., Weibring, P. and Wolfe, G. M.: Observing atmospheric formaldehyde
1242 (HCHO) from space: validation and intercomparison of six retrievals from four satellites (OMI, GOME2A,
1243 GOME2B, OMPS) with SEAC4RS aircraft observations over the Southeast US, Atmos. Chem. Phys., 0, 1–24,
1244 doi:10.5194/acp-2016-162, 2016.

1245 Zhou, Y., Brunner, D., Boersma, K. F., Dirksen, R., and Wang, P.: An improved tropospheric NO2 retrieval
1246 for OMI observations in the vicinity of mountainous terrain, Atmos. Meas. Tech., 2, 401-416, doi:10.5194/amt-
1247 2-401-2009, 2009.

1248 **APPENDIX A: Acronyms and abbreviations**

A	Averaging Kernel
AMF	Air mass factor
AOD	Aerosol optical depth
AAI	Aerosol absorbing index
ATBD	Algorithm Theoretical Basis Document
BIRA-IASB	Royal Belgian Institute for Space Aeronomy
BrO	Bromine Monoxide
BRDF	Bidirectional reflectance distribution function
CH_4	Methane
CO	Carbon Monoxide
CAPACITY	Composition of the Atmosphere: Progress to Applications in the user CommunITY
CCD	Charged Coupled Device
CF	Climate and Forecast metadata conventions
CRB	Clouds as Reflecting Boundaries
CTM	Chemical Transport Model
DOAS	Differential optical absorption spectroscopy
DU	Dobson Unit (1 DU = 2.6867×10^{16} molecules cm^{-2})
ECMWF	European Centre for Medium Range Weather Forecast
ESA	European Space Agency
FWHM	Full Width Half Maximum
GMES	Global Monitoring for Environment and Security
GOME	Global Ozone Monitoring Experiment
HCHO	Formaldehyde (or H_2CO)
IPA	Independent Pixel Approximation
IR	Infrared
ISRF	Instrument Spectral Response Function
L2	Level-2
L2WG	Level-2 Working Group
LER	Lambertian Equivalent Reflector
VLIDORT	Vector LInearized Discrete Ordinate Radiative Transfer
LOS	Line-of-sight angle
LS	Lower stratosphere
LUT	Look-up table
MAX-DOAS	Multi-axis DOAS
MPC	Mission Performance Center
NDACC	Network for the Detection of Atmospheric Composition Change
NMVOC	Non-Methane Volatile Organic Compound
NO_2	Nitrogen Dioxide

NRT	Near-real time
OCRA	Optical Cloud Recognition Algorithm
OD	Optical Depth
O_3	Ozone
OMI	Ozone Monitoring Instrument
OMPS	Ozone Mapping Profiler Suite
(P)BL	Planetary Boundary Layer
PCA	Principal Component Analysis
QA4ECV	Quality Assurance For Essential Climate Variables
RAA	Relative Azimuth Angle
ROCINN	Retrieval Of Cloud Information using Neural Networks
RRS	Rotational Raman Scattering
RTM	Radiative transfer model
S5P	Sentinel-5 Precursor
S5	Sentinel 5
SAA	Solar Azimuth Angle
SCIAMACHY	SCanning Imaging Absorption spectroMeter for Atmospheric ChartograpHY
SC(D)	Slant column density
SCDE	Slant column density error
SNR	Signal-to-noise ratio
SO_2	Sulfur dioxide
SOW	Statement Of Work
SWIR	Short-wave infrared
SZA	Solar zenith angle
TM 4/5	Data assimilation / chemistry transport model (version 4 or 5)
TROPOMI	Tropospheric Monitoring Instrument
UPAS	Universal Processor for UV/VIS Atmospheric Spectrometers
UV	Ultraviolet
UVN	Ultraviolet/Visible/Near-infrared
VAA	Viewing Azimuth Angle
VZA	Viewing Zenith Angle
VC(D)	Vertical column density

APPENDIX B: High level L2 HCHO data product description

In addition to the main product results, such as HCHO slant column, tropospheric vertical column and air mass factor, the level 2 data files contain a number of additional ancillary parameters and diagnostic information. **Error! Reference source not found.** A selection of important parameters is given in Table 13.

Table 13: Selective list of output fields in the TROPOMI HCHO product. Scanline and ground_pixel are respectively the number of pixels in an orbit along track and across track. Layer is the number of vertical levels in the averaging kernels and the a-priori profiles.

Symbol	Unit*	Variable name	Number of entries
N_v	mol.m^{-2}	formaldehyde_tropospheric_vertical_column	scanline x ground_pixel
N_s	mol.m^{-2}	fitted_slant_columns	scanline x ground_pixel x number_of_slant_columns
$N_s - N_{s,0}$	mol.m^{-2}	formaldehyde_slant_column_corrected	scanline x ground_pixel
$N_{v,0}$	mol.m^{-2}	formaldehyde_tropospheric_vertical_column_correction	scanline x ground_pixel
M	n.u.	formaldehyde_tropospheric_air_mass_factor	scanline x ground_pixel
M_{clear}	n.u.	formaldehyde_clear_air_mass_factor	scanline x ground_pixel
f_c	n.u.	cloud_fraction_crb	scanline x ground_pixel
w_c	n.u.	cloud_fraction_intensity_weighted	scanline x ground_pixel
p_{cloud}	Pa	cloud_pressure_crb	scanline x ground_pixel
A_{cloud}	n.u.	cloud_albedo_crb	scanline x ground_pixel
A_s	n.u.	surface_albedo	scanline x ground_pixel
z_s	m	surface_altitude	scanline x ground_pixel
$\sigma_{N,v,rand}$	mol.m^{-2}	formaldehyde_tropospheric_vertical_column_precision	scanline x ground_pixel
$\sigma_{N,v,syst}$	mol.m^{-2}	formaldehyde_tropospheric_vertical_column_trueness	scanline x ground_pixel
$\sigma_{N,s,rand}$	mol.m^{-2}	fitted_slant_columns_precision	scanline x ground_pixel x number_of_slant_columns
$\sigma_{M,rand}$	n.u.	formaldehyde_tropospheric_air_mass_factor_precision	scanline x ground_pixel
$\sigma_{N,s,0}$	mol.m^{-2}	formaldehyde_slant_column_corrected_trueness	scanline x ground_pixel
A	n.u.	averaging_kernel	layer x scanline x ground_pixel
n_a	vmr	formaldehyde_profile_apriori	layer x scanline x ground_pixel
p_s	Pa	surface_pressure	scanline x ground_pixel
a_l	Pa	tm5_constant_a	layer
b_l	n.u.	tm5_constant_b	layer

Symbol	Unit*	Variable name	Number of entries
$N_{s,1}$	mol.m^{-2}	fitted_slant_columns_win1	scanline x ground_pixel x number_of_slant_columns_win1
$\sigma_{N,s,1,rand}$	mol.m^{-2}	fitted_slant_columns_precision_win1	scanline x ground_pixel x number_of_slant_columns_win1

1256   * multiplication factor to convert mol.m^{-2} to molec.cm^{-2}: 6.022x10^{19}

APPENDIX C: Averaging Kernel

Retrieved satellite quantities always represent a weighted average over all parts of the atmosphere that contribute to the signal observed by the satellite instrument. The DOAS total column retrieval is implicitly dependant on the a priori trace gas profile n_a. Radiative transfer calculations account for the sensitivity of the measurement to the HCHO concentrations at all altitudes and these sensitivities are weighted with the assumed a priori profile shape to produce the vertical column. The averaging kernel (A) is proportional to the measurement sensitivity profile, and provides the relation between the retrieved column N_v and the true tracer profile x (Rodgers, 2000; Rodgers and Connor, 2002):

$$N_v - N_{v,a} = A.(x^{pc} - n_a^{pc}) \tag{21}$$

where the profiles are expressed in partial columns (pc). For total column observations of optically thin absorbers DOAS averaging kernels are calculated as follows (Eskes and Boersma, 2003): $A(p) = \frac{m(p)}{M}$, where $m(p)$ is the altitude-resolved air mass factor and M is the tropospheric air mass factor. The air mass factor and therefore the retrieved vertical column, depends on the a priori profile shape, in contrast to the altitude-resolved air mass factor which describes the sensitivity of the slant column to changes in trace gas concentrations at a given altitude and does not depends on the a priori profile in an optically thin atmosphere. From the definition of A, we have $N_{v,a} = A.n_a^{pc}$ and Equation (21) simplifies to:

$$N_v = A.x^{pc} \tag{22}$$

The averaging kernel varies with the observation conditions. In the HCHO retrieval product, A is provided together with the error budget for each individual pixel. The provided HCHO vertical columns can be used in two ways, each with its own associated error (Boersma et al., 2004):

1. For independent study and/or comparison with other independent measurements of total column amounts. In this case, the total error related to the column consists of slant column measurement errors, reference sector correction errors, and air mass factor errors. The latter consists of errors related to uncertainties in the assumed profile n_a and errors related to the m parameters.

2. For comparisons with chemistry transport models or validation with independent profile measurements, if the averaging kernel information is used, the a priori profile shape error no longer contributes to the total error. Indeed, the relative difference between the retrieved column N_v and an independent profile x_i is:

$$\delta = \frac{N_v - A.x_i^{pc}}{N_v} \tag{23}$$

1284   The total AMF M cancels since it appears as the denominator of both N_v and A. Because only the total

1285   AMF depends on the a priori tracer profile n_a, the comparison using the averaging kernel is not influenced

1286   by the chosen a priori profile shape. The a priori profile error does not influence the comparison, but of

1287   course, it still does influence the error on the retrieved vertical column.